Chapter 5. Production of high-purity $CaCO_3$ *via* an indirect calcium sulphide carbonation process

Indirect mineral carbonation involves two separate steps, in which the reactive component (basic metal, for example calcium or magnesium ions) is first leached out from the mineral or waste matrix by a leaching medium, followed by carbonation in a separate step (Teir et al. 2005). If calcium could be selectively extracted from the waste matrix prior to carbonation, a pure, high-value marketable PCC can be produced (Said et al. 2013; Eloneva et al. 2009; Lu et al. 2009; Teir et al. 2007).

The advantage of this approach over the direct aqueous CaS carbonation process (Chapter 4) is that each individual step can be optimized separately, incorporating further steps if needed. In addition, the adoption of this dual approach (i.e. direct *vs* indirect) provided further insight into the conditions at which $CaCO_3$ of different grades can be produced.

Two process configurations for the production of high-purity $CaCO_3$ from CaS via indirect mineral carbonation were studied at ambient temperature and pressure. First, CO_2 gas was used to induce CaS dissolution and generated a Ca-rich solution, whilst the second configuration made use of H_2S gas. In the second step of the process, the particulate-free, Ca-rich solution was used to produce $CaCO_3$ of high purity. Only the effect of gas flow-rate and the mode of mixing, mechanical agitation and ultrasound irradiation, on the reaction kinetics were investigated, along with their effects on the crystal structure and polymorphs of the carbonate products formed.

5.1 Outline of the indirect CaS carbonation process

An outline of the indirect CaS carbonation process is illustrated schematically in Figure 5.1 (the areas highlighted in red represent the focus of this chapter). Waste gypsum ($CaSO_4.2H_2O$) was first thermally reduced to calcium sulphide (CaS) (Mbhele et al. 2009; Ruto et al. 2011). The CaS solid sample formed was subjected to aqueous dissolution, carbonation and stripping in a two-step process. Either CO_2 gas (Figure 5.1 a) or H_2S gas (Figure 5.1 b) was used to induce CaS dissolution.

In the carbonation process where CO_2 gas was used for the dissolution of CaS particles, the initial carbonation reaction was interrupted as soon as CaS dissolution was completed in order to remove solid residues and produce a particulate-free, Ca-rich solution. The latter was subsequently used to produce $CaCO_3$ of a high level of purity. The processes of CaS dissolution and H_2S stripping/calcium carbonation were separated by a filtration step.

In the second carbonation process, H_2S gas was used for the dissolution of solid CaS particles. H_2S gas dissolves in water to produce aqueous H_2S which reacts with the CaS to form a highly soluble $Ca(HS)_2$ solution (Eq. (5.1).

$$CaS\ (s) + H_2O\ (l) + H_2S\ (aq) \rightarrow Ca(HS)_2 + H_2O\ (l); \quad \Delta H_{25°C} = -44.8\ kJ \qquad (5.1)$$

Upon complete dissolution of CaS, the solid residue was removed by filtration and the particulate-free, Ca-rich solution was contacted with gaseous CO_2 to produce high-purity $CaCO_3$.

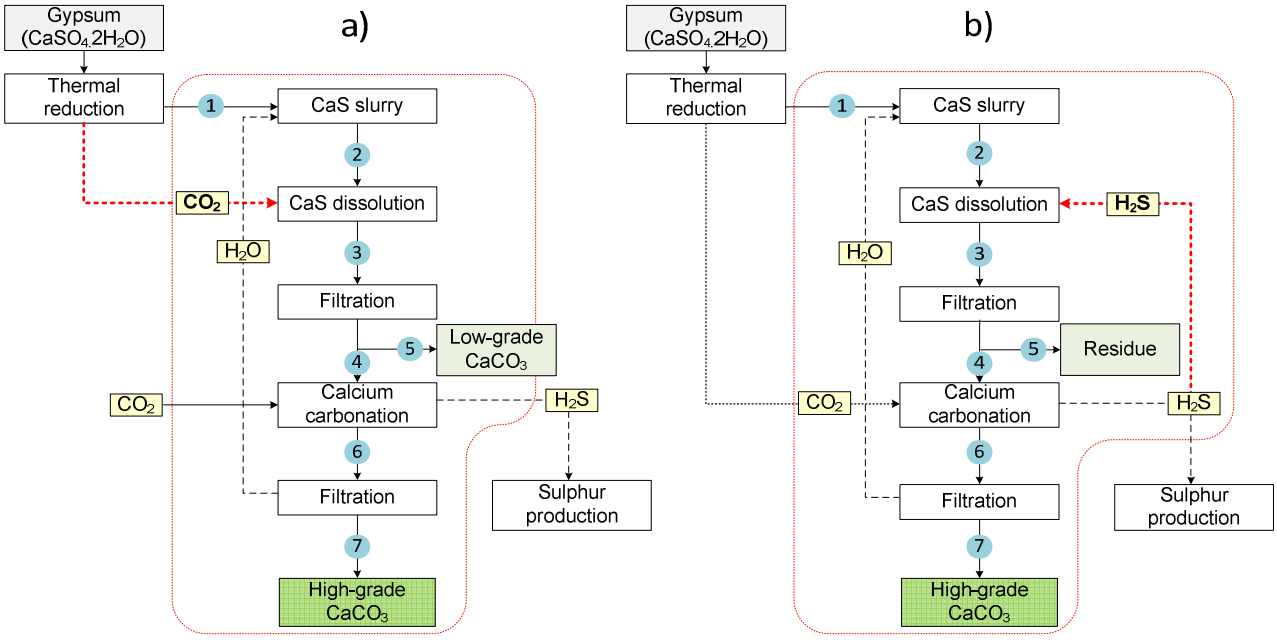

Figure 5.1 Suggested processes for the production of high-grade $CaCO_3$ from waste gypsum *via* indirect CaS carbonation using a) CO_2 gas or b) H_2S gas for CaS dissolution: 1) CaS solids; 2) CaS slurry; 3) $Ca(HS)_2$ solution (before filtration); 4) $Ca(HS)_2$ solution (filtered); 5) Secondary product or waste stream; 6) $CaCO_3$ slurry; 7) high-grade $CaCO_3$ product.

5.2 Materials and Methods

Feedstock

The CaS used as the raw material was a calcine product produced from waste gypsum generated at an acid mine water neutralisation plant (Materials and Methods, p. 33). The degree of purity of the calcine sample, expressed as % CaS, was determined by X-ray diffraction and a wet analytical method (Appendix A.2.1.).

Experimental procedure

The dissolution reactions were performed in either 1 or 3-litre Perspex stirred tank, batch reactors using the experimental set-up described in Chapter 3 (pp. 34-36 of this document). For conventional mixing with the CSTR reactor, a mechanical overhead stirrer (RW 20 Digital, from IKA®-Werke GmbH & Co. KG, Germany; Appendix A.1.3) and a Rushton turbine impeller (manufactured by Manten Engineering, South Africa) were used. Carbonation reactions were performed in either a 1-litre CSTR reactor equipped with an overhead stirrer, or 1-litre glass beakers (Pyrex Brand tall form; 187 × 89 mm) using either mechanical agitation (magnetic stirrer with a PTFE-coated magnetic stirrer bar at 730 min^{-1}; RCT basic IKAMAG® safety control, IKA Works Inc, Germany; Appendix A.1.4) or ultrasound irradiation (Hielscher UP400S ultrasonic processor, Hielscher Ultrasonics GmbH, Germany; Appendix A.1.5) for mixing.

Depending on the experimental matrix, the required amount of calcine was dispersed in distilled water to obtain a pre-determined slurry concentration. After 30 min of continuous mixing, CO_2 gas or H_2S gas was introduced at a constant flow-rate into the slurry via a sparger to induce CaS conversion and dissolution. The pH, electrical conductivity and temperature of the suspension in the reactor were logged at 5 second intervals to monitor the reaction profile and kinetics. Filtered samples of the CaS suspension were collected from the reactor at regular intervals. The filtrates were analysed for their calcium contents.

- For the CO_2 dissolution experiments, as soon as the electrical conductivity of the suspension, which was used as an indirect indicator of the concentration of solubilized anions and cations, reached the maximum value, the reaction was stopped by shutting off the CO_2 gas flow. The conductivity of the solution was measured at 5 sec intervals, using the multi-parameter logging unit with a display unit. The suspension was immediately removed from the reactor and the solids removed by vacuum filtration using Whatman No. 1 filter paper. The solid was washed twice with distilled water and dried at 60°C for at least 24 hours. The filtrate, $Ca(HS)_2$ solution, was reacted with CO_2. The effect of various CO_2 flow-rates on the reaction kinetics and the characteristics of the final product were investigated.
- For the H_2S dissolution experiments, the same experimental procedure was followed, except that the reaction was terminated by shutting off the H_2S gas flow when the pH and electrical conductivity remained unchanged for 10 to 15 min. Upon completion, the suspension was removed by vacuum filtration (Whatman No. 1 filter paper), washed twice with distilled water and dried at 60°C for at least 24 hours. The filtrate ($Ca(HS)_2$ solution) was transferred into a 1-litre glass beaker for further reaction with CO_2. The effect of stirring mode (mechanical

agitation *versus* ultrasound irradiation) and CO_2 flow-rate on the reaction kinetics and the characteristics of the final products were studied.

Since ultrasound is deemed to promote the precipitation of different $CaCO_3$ polymorphs (Santos et al. 2012), the effect of stirring mode was investigated. The $Ca(HS)_2$ carbonation reactions were done using either mechanical agitation (magnetic stirrer) or ultrasound irradiation, for mixing. For the ultrasound irradiation studies, a Hielscher UP400S ultrasonic processor, which operates at 24 kHz frequency and delivers 400 W gross power, was used. The probe used was an H3 standard sonotrode horn, which had a tip diameter of 3 mm, maximal amplitude of 210 µm, and an acoustic power density of 460 W/cm^2. The adjustable amplitude and pulse were maintained at 100%. The horn was immersed in the centre of the reaction solution at a depth of 10 mm below the liquid surface. The temperature of the reaction mixture was monitored (logged at 5 second intervals) throughout the experimental runs but was not externally controlled to maintain a constant temperature since temperature control was not included in the initial experimental matrix (follow-up study). The total amount of energy (E) delivered to a suspension not only depends on the applied power (P) but also on the total amount of time (t) that the suspension was subjected to the ultrasonic treatment.

$$E = P \times t \qquad (5.3)$$

While sonication power and time describe the amount of energy delivered to the suspension, samples of different volumes particle concentrations can respond differently to the same amount of delivered energy. The effective delivered power is calculated using the following equation:

$$P = dT/dt \times M \times C_p \qquad (5.4)$$

Where P is the delivered power (W), T and t are temperature (Kelvin) and time (seconds), respectively, C_p the specific heat of the liquid (J/g.K) and M the mass of the liquid (g). [x]

After 10 min of continuous mixing (mechanical agitation or ultrasound irradiation) of the filtrate from the CaS dissolution step, CO_2 gas was introduced at a constant flow-rate via a sparger in order to precipitate high-grade $CaCO_3$ in the calcium carbonation step. The pH, electrical conductivity and temperature of the suspension in the reactor were logged at 5 second intervals to monitor the reaction progress.

Sub-samples (20 mℓ) of the Ca-rich solution were also collected from the reactor at regular intervals and filtered using 0.45µm PALL acrodisc PSF GxF/GHP membranes (Microsep (Pty) Ltd, South Africa). The filtrates (undiluted, acidified samples) were analysed for their calcium contents by an accredited laboratory. The reaction was terminated when the pH and electrical conductivity remained unchanged for 10 to 15 min, indicating the completion of the reaction. Immediately upon completion of the experimental run, the final suspension was removed from the reactor by vacuum filtration using 0.45µm Millipore HA membranes (Microsep (Pty) Ltd, South Africa) and washed twice with distilled water. The filter cakes consisting of high-grade $CaCO_3$ were dried at 60°C for 24 h.

The flow-chart for the experimental procedure for CaS dissolution and calcium carbonation is given in Figure 5.2.

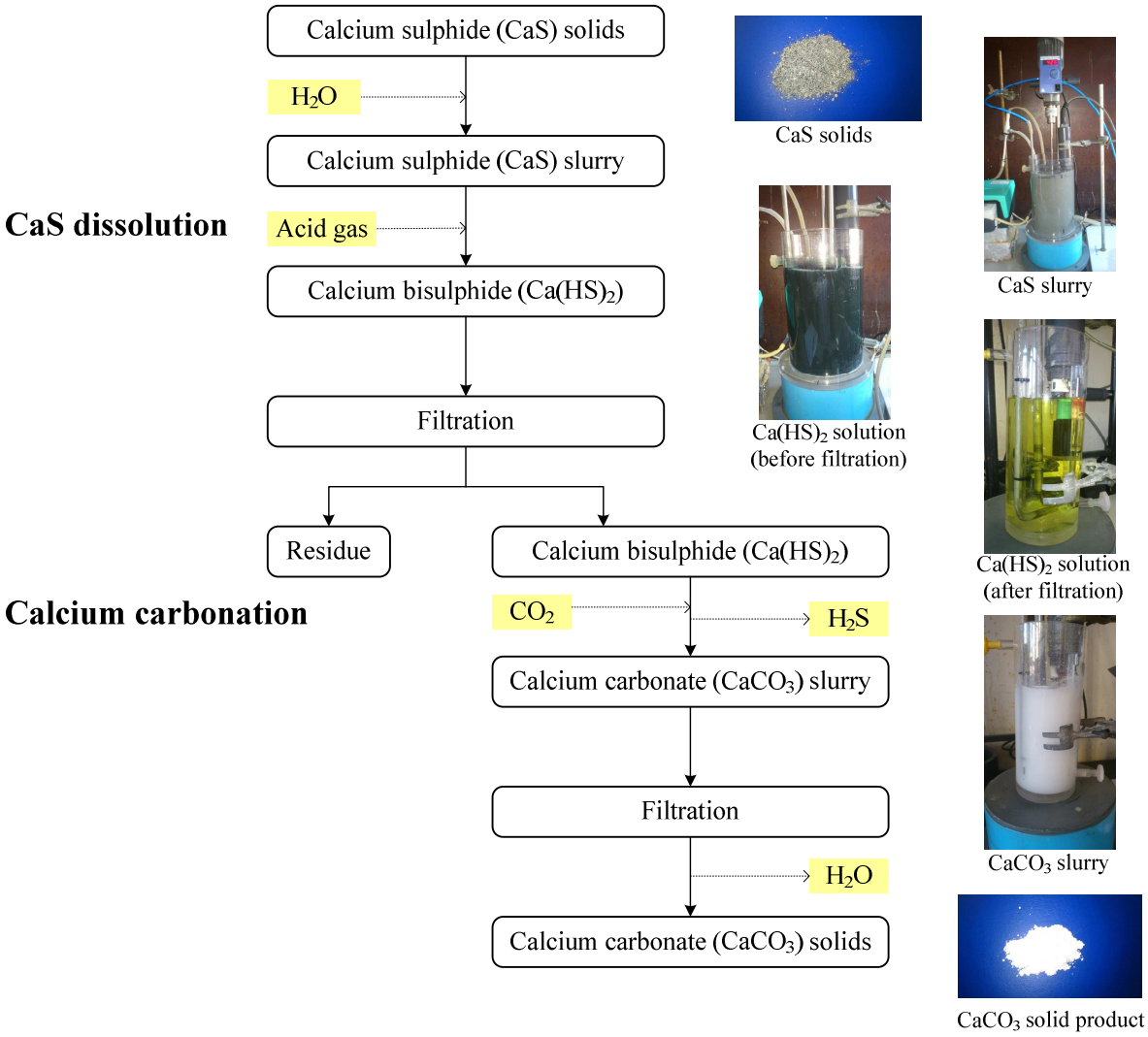

Figure 5.2 Flow-chart of the experimental procedure for the production of high-purity $CaCO_3$ from CaS.

Analytical

The pH, temperature and electrical conductivity of the suspension contained in the reactors were recorded over time throughout the dissolution/stripping/carbonation process using a Hanna HI 2829 multi-parameter logger set at 5 second measurement intervals. The concentration of calcium ions in solution was determined by inductively coupled plasma mass spectrometry (ICP-MS) at an accredited laboratory (Consulting and Analytical Services, CSIR, Pretoria, South Africa).

The solid samples were characterised by XRD, ATR-FTIR and SEM. The particle size analysis, specific surface area, pore volume, and bulk density of the solid samples were determined (detailed methods or techniques are described in Chapter 3 (pp. 39-42 of this document)).

5.3 Results and Discussion

The CaS content/purity of the calcine feed material was shown to be 81.7 ± 0.83 % (as CaS) (Wet analytical method; Appendix A.2.1). The bulk mineralogical composition of the untreated calcine sample was determined by XRD. The relative phase amounts (mass%) were estimated using the Rietveld method and the main mineral present in the sample was found to be calcium sulphide (CaS; 83.0 %), also called oldhamite, which confirmed the efficiency of the thermal reduction process of the waste gypsum. Less abundant mineral phases included hydroxyapatite (8.17 mass%), quartz (4.32 mass%), anhydrite (4.19 mass%), and lime (0.31 mass%). Error defined as 3 standard deviations are given in Table 5.1. The XRD diffractogram and SEM images of the calcine feed material are reported in the Supplementary Information S5.1, pp. 124-125.

Table 5.1 Mineral composition of the calcine feed material used during the indirect CaS carbonation process

Name	**Formula**	**Mass (mass%)**	**Error (mass%)**
Anhydrite	$CaSO_4$	4.19	0.69
Lime	CaO	0.31	0.11
Hydroxyapatite	$Ca_{8.86}(PO_4)_6(H_2O)_2$	8.17	0.54
Oldhamite	CaS	83.01	0.90
Quartz	SiO_2	4.32	0.51

The calcine sample was subjected to aqueous dissolution, carbonation and stripping in a two-step (indirect) process.

5.3.1 Indirect CaS carbonation using CO_2 gas for CaS dissolution

A simplified schematic diagram, including the chemical reactions, of the indirect CaS carbonation process using CO_2 gas for CaS dissolution is shown in Figure 5.3. Based on the carbonate content, a carbonate material is generally classified as low-grade $CaCO_3$ if the carbonate content is less than 90 mass% $CaCO_3$ and as high-grade $CaCO_3$ if it is greater than 99 mass% as $CaCO_3$ (Oates 1998).

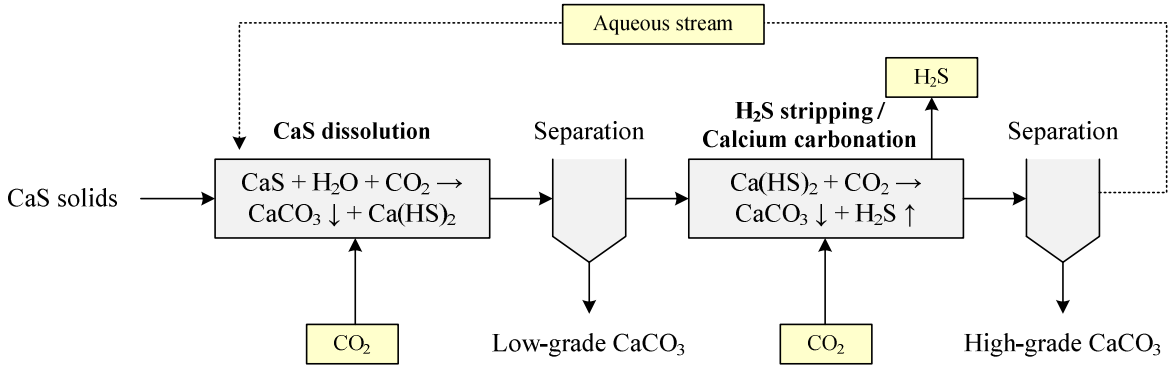

Figure 5.3 Indirect CaS carbonation processes for the production of two different grades of $CaCO_3$, using CO_2 gas for CaS dissolution

The experimental conditions, mineral composition and $CaCO_3$ yields are shown in Table 5.2. Although high-grade $CaCO_3$ (> 99 mass% as $CaCO_3$) products could be produced in the second step of the process, the percentage yield of these products were very low, and varied between 12 and 23 %. The majority of the Ca-ions from the CaS feed material precipitated as $CaCO_3$ in the first step together with solid impurities to produce high yields of low-value, low-grade $CaCO_3$ products (< 90 mass% as $CaCO_3$). Approximately 0.98 kg low-grade $CaCO_3$ and 0.14 kg high-grade $CaCO_3$ were produced for every 1 kg CaS processed.

Completion of the CaS dissolution reaction was monitored via the electrical conductivity of the suspension and as soon as it had reached a maximum value, the reaction was stopped. The big variation in the percentage yield of the high-grade $CaCO_3$ can be ascribed to the difficulty in determining the exact end point of the CaS dissolution step.

Table 5.2 Mineral composition of the products generated in the indirect CaS carbonation process route when CO_2 gas was used for CaS dissolution

CaS dissolution step							
Experimental conditions	Sample ID		M33	M35	M53	M81	M84
	CaS slurry	%	4	4	4	5	5
	Volume	mℓ	700	700	700	3000	3000
	Calcine mass	g	28.0	28.0	28.0	150.0	150.0
	Calcium	mmol/ℓ	450	450	450	560	560
	Initial pH		12.1	12.4	11.8	11.8	11.7
	Gas flow-rate	ℓ CO_2/min/kg calcine	40.0	15.7	50.0	2.9	12.7
	Stirring	min^{-1}	1050	1045	1000	580	580
Low-grade $CaCO_3$							
Mineral composition	Calcite	%	71.66	87.38	74.8	87.44	46.49
	Vaterite	%	15.67	2.06	13.97	0.85	31.32
	Fluorite	%	1.81	1.66	1.19	1.86	1.45
	Quartz	%	1.19	1.19	0.98	1.69	2.25
	Apatite	%	6.28	5.4	5.45	6.38	6.65
	Anhydrite	%	2.23	1.98	1.95	9.27	11.85
	Oldhamite	%	1.16	0.34	1.66	1.51	-
Actual yield		g	27.64	22.61	27.17	127.88	137.33
H_2S stripping step/calcium carbonation							
Experimental conditions	Number		M34	M36	M54	M82	M85
	Initial pH		9.1	8.5	8.1	10.2	10.5
	Initial Ca	mmol/ℓ	55	69	55	130	106
	Volume	mℓ	700	700	700	3000	3000
	Gas flow-rate	ℓ CO_2/min	1.12	0.50	1.90	0.44	1.90
	Stirring	min^{-1}	1050	1040	1000	580	580
High-grade $CaCO_3$							
Mineral composition	Calcite	%	99.47	99.49	98.60	99.41	100.0
	Quartz	%	0.53	0.51	0.49	0.50	-
	Sulphur	%	-	-	0.90	0.10	-
Theoretical yield		g	31.658	31.658	31.704	169.598	169.598
Actual yield		g	3.810	4.830	3.835	38.988	31.817
Percentage yield		%	12.03	15.26	12.10	22.99	18.76

The low-grade $CaCO_3$ product generated in the first step of the process was greyish-white in colour (Figure 5.4 (a)) whilst the high-grade $CaCO_3$ was a pure white product (Figure 5.4 (b)). Differences in the particle size analysis were also noted. The mode size represents the particle size most commonly found in the particle size distribution and was 14.23 µm for the low-grade $CaCO_3$ and 32.0 µm for the high-grade $CaCO_3$. The D10, D50 and D90 parameters refer to the cumulative size distributions which describes how many percentages of the particles in the sample are below a certain size. For the low-grade $CaCO_3$, the D10, D50 and D90 values were 6.1 µm, 15.3 µm and 41.7 µm and for the high-grade $CaCO_3$, 23.3 µm, 32.3 µm and 46.1 µm, respectively. The high-grade $CaCO_3$ are generally of larger size and with a narrow particle size distribution compared to the low-grade $CaCO_3$ product.

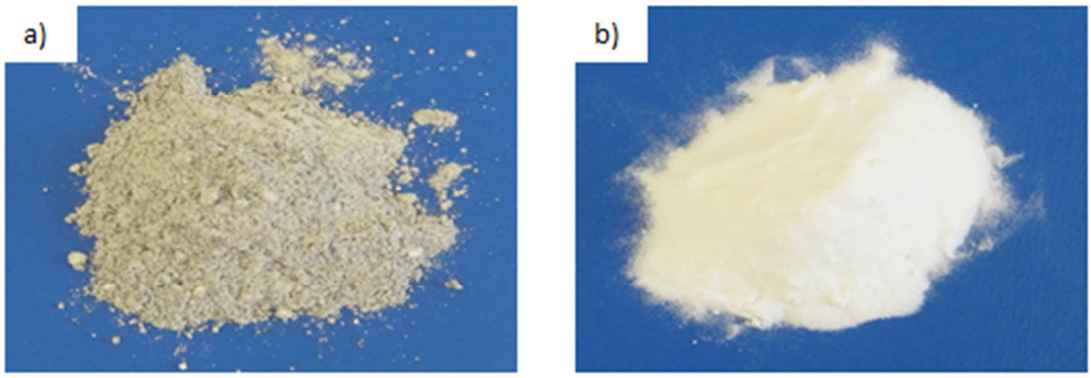

Figure 5.4 Photographs of a) low-grade $CaCO_3$ and b) high-grade $CaCO_3$ produced in the first and second steps, respectively, of the indirect carbonation process using CO_2 gas for CaS dissolution

XRD, FTIR spectroscopy and SEM were employed to study the crystal structure/s or polymorph phase/s of the high-grade $CaCO_3$ particles. Figure 5.5 shows the XRD diffraction pattern of the high-grade $CaCO_3$ particles and were revealed to be 99.5 mass% calcite and 0.5 mass% quartz. Chakraborty et al. (1996) reported that the type of crystalline form is dependent on the supersaturation level and ionic ratio of $[Ca^{2+}]/[CO_3^{2-}]$ in solution. The fundamental experimental conditions for obtaining rhombohedral calcite consist of relatively low-concentration of both CO_3^{2-} and Ca^{2+} ions. Since most of the calcium ions precipitated in the first step, as low-grade $CaCO_3$, only diluted calcium containing solutions (< 130 mmol/ℓ, Table 5.2) were available for the carbonation reaction in the second step. As a result, only calcite crystals were formed in the second step of the indirect CaS carbonation process when CO_2 gas was used for CaS dissolution.

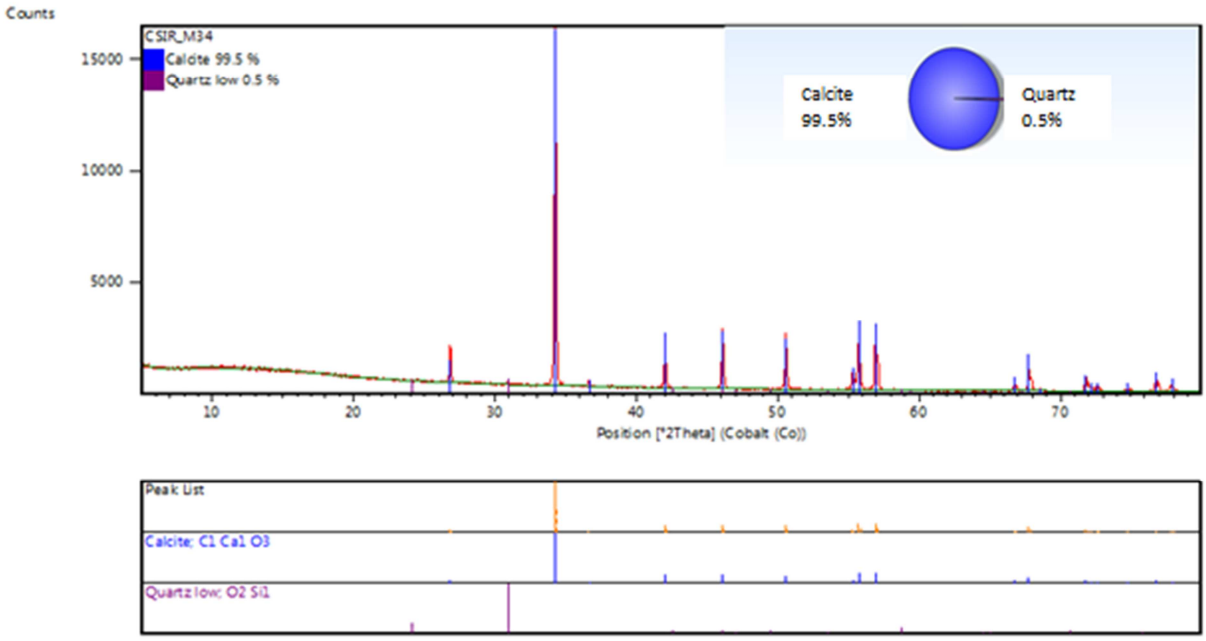

Figure 5.5 XRD diffraction pattern and mineral composition of the high-grade $CaCO_3$ produced in the second step of the indirect CaS carbonation process using CO_2 gas for CaS dissolution. (Ca-rich solution containing 55 mmol/ℓ as Ca; initial pH: 9.05; stirring rate: 1050 min^{-1}; gas flow-rate: 1.12 ℓ CO_2/min; 1ℓ CSTR reactor)

The FTIR spectrum (Figure 5.6) of the products revealed the characteristic transmittance peaks of calcite, which are the in-plane band and the out-plane band at 713 cm^{-1} and 873 cm^{-1}, respectively, and the anti-symmetry stretch at around 1400 cm^{-1} (Menahem & Mastai 2008; Xu et al. 2011). The presence of the calcite phase alone was confirmed by the identification of the characteristic υ_4 band of calcite at 713 cm^{-1} and the absence of the characteristic υ_4 band of vaterite at 745 cm^{-1}.

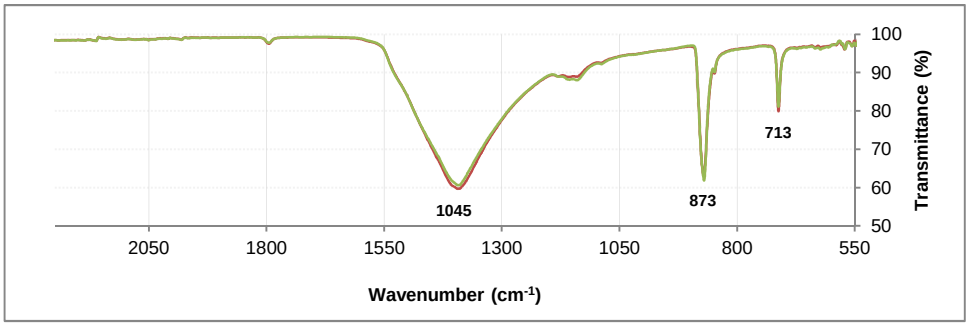

Figure 5.6 FT-IR transmission spectrum of the high-purity $CaCO_3$ formed in the second step of the process. (Ca-rich solution containing 55 mmol /ℓ as Ca; initial pH: 9.05; stirring rate: 1050 min^{-1}; gas flow-rate: 1.12 ℓ CO_2/min; 1ℓ CSTR reactor)

The morphology of the high-grade $CaCO_3$ is illustrated in Figure 5.7. A precipitate was produced of spherical micron-sized, interpenetrated rhombohedral cubes of calcite (Ma & Feng 2011) with smooth surfaces. Laser scattering particle size distribution analysis is presented in Figure 5.8, confirming the micron-sized particle size (geometric mean size 31.85 ± 1.59 µm).

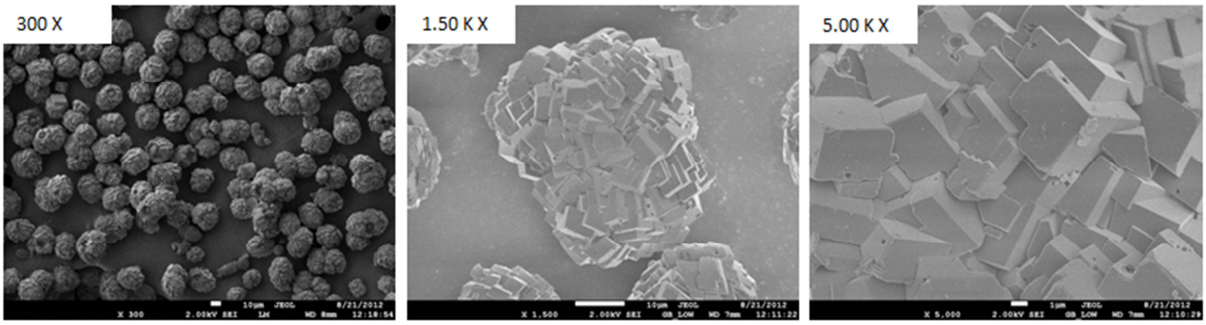

Figure 5.7 SEM images of the high-purity $CaCO_3$ produced by the indirect carbonation process using CO_2 gas for CaS dissolution. (Ca-rich solution containing 55 mmol /ℓ as Ca; initial pH: 9.05; stirring rate: 1050 min^{-1}; gas flow-rate: 1.12 ℓ CO_2/min; 1ℓ CSTR reactor)

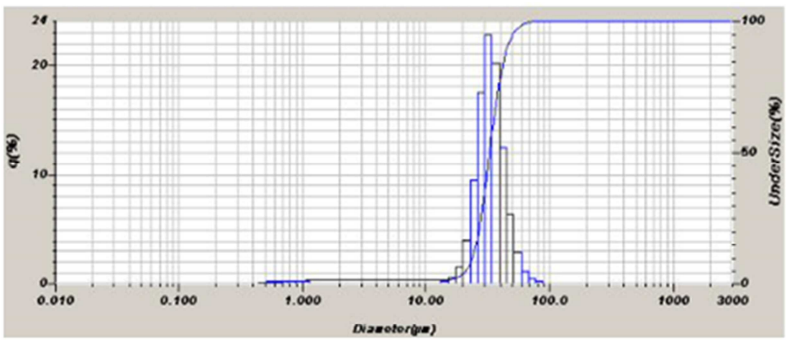

Median size : 32.9072 (µm)
Mean size : 33.9293 (µm)
Std dev. : 9.6682 (µm)
Geo. mean size : 31.8501 (µm)
Geo. std dev. : 1.5979 (µm)
Mode size : 32.2744 (µm)
Diameter on cumulative %
: (1) 10.00 %: 23.7054 (µm)
: (2) 30.00 %: 28.9827 (µm)
: (3) 40.00 %: 30.9981 (µm)
: (4) 50.00 %: 32.9072 (µm)
: (5) 60.00 %: 35.0233 (µm)
: (6) 70.00 %: 37.4705 (µm)
: (7) 80.00 %: 40.6299 (µm)
: (8) 90.00 %: 45.7198 (µm)
: (9) 95.00 %: 50.9034 (µm)

Figure 5.8 Laser scattering particle size distribution analysis of the high-purity $CaCO_3$ produced during the carbonation step. (Ca-rich solution containing 55 mmol/ℓ as Ca; initial pH: 9.05; stirring rate: 1050 min^{-1}; gas flow-rate: 1.12 ℓ CO_2/min; 1ℓ CSTR reactor)

The effect of the CO_2 gas flow-rate on the surface characteristics of $CaCO_3$ crystals was also investigated. Table 5.3 shows the measured surface area and density and Figure 5.9 provides details on the morphology and surface area of the products produced at two different CO_2 gas flow-rates. Although the two products generated at different CO_2 gas flow-rates exhibited an identical density of 2.72 g/cm^3, which is characteristic of calcite (Plummer & Busenberg 1982), distinct appearances of the crystal surface were evident (Figure 5.9). At the lower CO_2 flow of 0.44 ℓ CO_2/min, the surfaces of the calcite particles produced were mostly observed as being rough and imperfect (Figure 5.9 (a)), with measured surface areas of 1.95 ± 0.02 m^2/g. At the higher CO_2 flow-rate of 1.90 ℓ CO_2/min, the surfaces of the calcite particles were generally smoother with sharper edges (Figure 5.9 (b)) and the measured surface area was also lower at 1.19 ± 0.01 m^2/g.

Table 5.3 Effect of CO_2 flow-rate on the surface area and density of the $CaCO_3$ products. (Initial pH: 10.5; stirring rate: 580 min^{-1}; 3ℓ CSTR reactor)

CO_2 flow-rate (ℓ/min)	**Ca-rich solution (mmol/ℓ as Ca)**	**BET surface area (m^2/g)**	**Density (g/cm^3)**	**Sample ID**
0.44	130	1.95 ± 0.02	2.72 ± 0.004	M82
1.90	106	1.19 ± 0.01	2.72 ± 0.003	M85

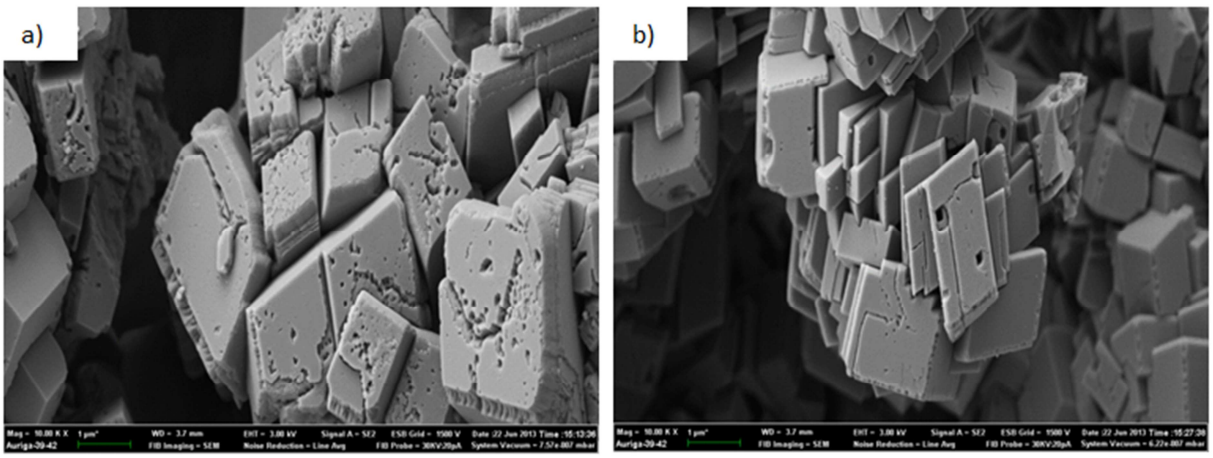

Figure 5.9 Scanning electron micrographs (10000 × magnification) of $CaCO_3$ crystals produced at CO_2 flow-rates of a) 0.44 ℓ/min and b) 1.90 ℓ/min respectively. (Initial pH: 10.5; stirring rate: 580 min^{-1}; 3ℓ CSTR reactor)

The high-grade $CaCO_3$ produced in the second step of the indirect carbonation process, using CO_2 gas for dissolution, were interpenetrated rhombohedral cubes of calcite. The particles produced at higher CO_2 flow-rates showed crystals with smoother surfaces, sharper edges but lower total surface area compared to products generated at lower CO_2 flow-rates. SEM micrographs at lower magnifications, of the high-grade $CaCO_3$ produced at 0.44 and 1.90 ℓ CO_2/min, are available in the Supplementary Information S5.2, p. 121.

5.3.2 Indirect CaS carbonation using H_2S gas for CaS dissolution

A simplified schematic diagram, including the chemical reactions, of the indirect CaS carbonation process, using H_2S gas for CaS dissolution, is shown in Figure 5.10.

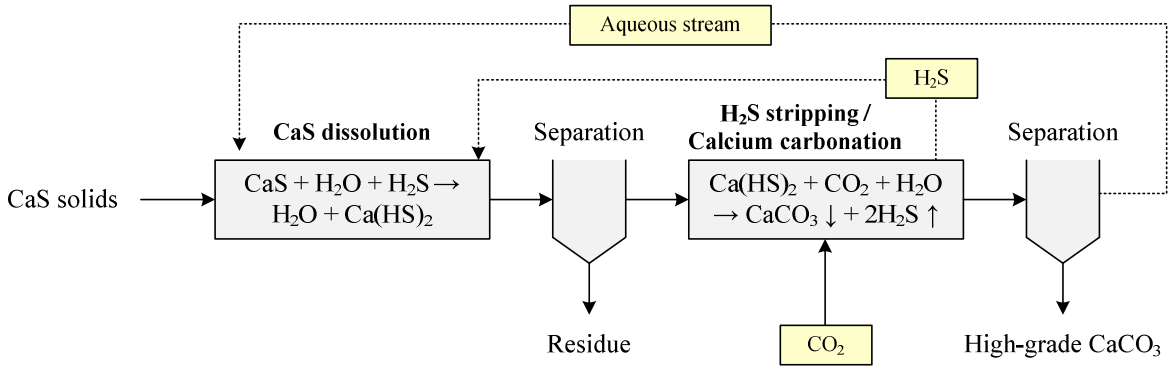

Figure 5.10 Indirect CaS carbonation process for the production of high-grade $CaCO_3$, using H_2S gas for CaS dissolution

CaS dissolution using H_2S gas

The effect of the H_2S gas flow-rate on the CaS dissolution reaction was investigated by monitoring the profile of several parameters over time: the pH (Figure 5.11 (a)), change in reactor temperature (Figure 5.11 (b)), and change in solubilised calcium concentration (Figure 5.11 (c)) at three different H_2S gas flow-rates (0.68, 1.26, and 1.89 ℓ H_2S/min). Although these results showed that an increase in the H_2S gas flow-rate accelerated the overall reaction and shortened the CaS dissolution time, the mole ratio of H_2S to Ca^{2+} needed for complete dissolution of CaS was constant at 0.68 (Figure 5.12). Complete dissolution was indicated by the levelling off of the drop in pH.

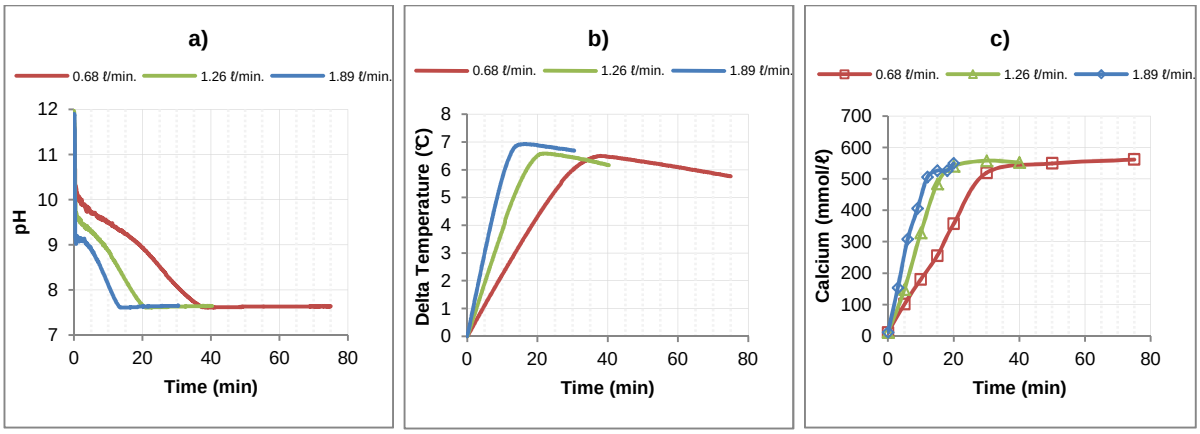

Figure 5.11 Effect of the H_2S gas flow-rate on the a) pH, b) change in reaction temperature and c) change in soluble calcium concentration of the CaS dissolution reaction with time. (CaS slurry containing 22.5 g /ℓ as Ca; initial pH: ~11.9; stirring rate: 700 min^{-1})

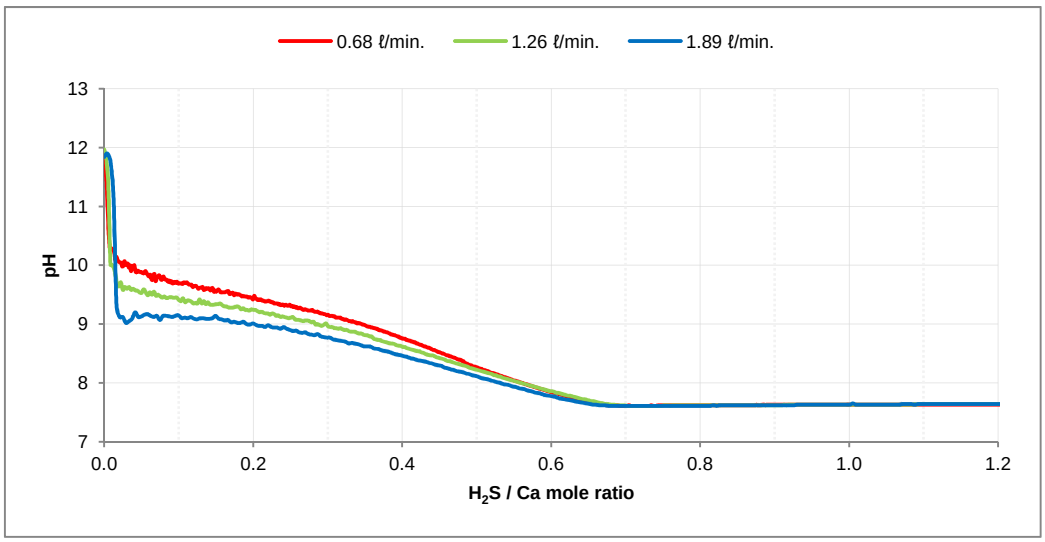

Figure 5.12 Effect of H_2S gas flow-rate on the mole ratio of H_2S to calcium required for complete CaS dissolution (Ca-rich solution containing 22.5 g/ℓ as Ca; initial pH: ~11.9; stirring rate: 700 min^{-1})

A summary of the calculated rate constants at the different H_2S gas flow-rates is presented in Table 5.4. At an H_2S flow-rate of 0.68 ℓ/min, the CaS dissolution rate was 16.92 mmol Ca/ℓ/min and the reaction was complete within about 33 min. At an H_2S flow-rate of 1.26 ℓ/min, the rate constant was 31.92 mmol Ca/ℓ/min and the reaction was complete within about 18 min, and at an H_2S flow-rate of 1.89 ℓ/min, the rate increased to 44.46 mmol Ca/ℓ/min and the reaction reached completion within about 13 min The calculated rate constants confirmed faster CaS dissolution times taking place with increased H_2S flow-rates.

Table 5.4 Reaction kinetics of the CaS dissolution reaction using H_2S gas (CaS slurry containing 22.5 g /ℓ as Ca)

H_2S flow (ℓ/min)	**Initial reaction conditions**			**Reaction kinetics**			**Reaction time (min)**
	Soluble calcium (mmol/ℓ)	**pH**	**Mixing rate (min^{-1})**	**Rate constant (mmol/ℓ/min as Ca)**	**Standard deviation (±)**	**R^2**	
0.68	11	11.78	700	16.92	0.48	0.9975	33
1.26	4	11.97	700	31.92	1.14	0.9975	18
1.89	20	11.84	700	44.46	2.8	0.9921	13

The residue generated in the first step of the indirect carbonation process, using H_2S gas for CaS dissolution, was dark grey in colour (Figure 5.13). The experimental conditions, particle analysis and actual yields of the residues generated from CaS dissolution using H_2S gas at various flow-rates are shown in Table 5.5 and detailed particle size distributions in Figures 5.14.

Figure 5.13 Photograph of residue generated in the first step of the indirect carbonation process using H_2S gas for CaS dissolution.

The dissolution of CaS (as a 5% slurry) using H_2S gas, generated a residue in the first step that was dark grey in colour and a 'Ca-rich' filtrate containing 560 mmol/ℓ as Ca. In comparison, when CO_2 gas was used for CaS dissolution, a low-grade $CaCO_3$ was formed in the first step that was lighter in colour (greyish-white) and a 'Ca-rich' filtrate containing 106 mmol/ℓ as Ca.

Table 5.5 Actual yields and particle size analysis of the residues produced at the end of Step 1 as a result of CaS dissolution using H_2S gas

CaS dissolution using H_2S gas : Residue generation					
Experimental conditions	Sample ID		M92	M93	M91
	CaS slurry	%	5	5	5
	Calcine mass	g	150.0	150.0	150.0
	Volume	mℓ	3000	3000	3000
	Initial pH		11.78	11.97	11.84
	Gas flow-rate	ℓ H_2S/min	0.96	1.26	1.89
	Stirring	min^{-1}	700	700	700
Particle size analysis		median size, D50 (µm)	12.17	14.30	11.64
		mode size (µm)	10.85	12.42	12.31
		D10 (µm)	5.10	6.30	5.30
		D90 (µm)	107.1	64.4	34.1
Actual yield		g	64.38	67.28	62.47

While the reaction was more rapid with increased H_2S flow-rates (Table 5.4), the particle size analyses of the residues formed were not very different in terms of their median and mode sizes (Table 5.5 and Supplementary Information S3, p. 122). The median size, also known as D50, is the particle size in microns where 50% of the population lies above and below this value. The mode size represents the particle size most commonly found in the particle size distribution (Figure 5.14).

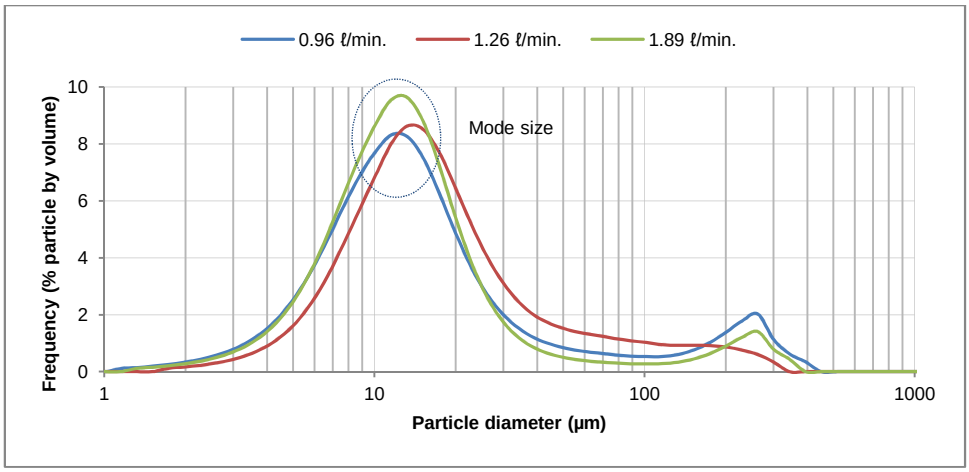

Figure 5.14 Particle size frequency distribution of the residues generated at various H_2S flow-rates

The D10, D50 and D90 parameters refer to the cumulative size distributions which describes how many percentages of the particles in the sample are below a certain size (Table 5.5). For the residue generated at 0.96 ℓ H_2S/min, the D10 was 5.1 µm, the D50, 12.2 µm and the D90, 107.1 µm which meant that 10% of the particles were below 5.1 µm, 50% below 12.2 µm (i.e., the median diameter) and 90% of the particles were below 107.1 µm. Increasing the H_2S flow-rate had a significant influence on the D90 value (Table 5.5). At H_2S flow-rates of 0.36, 1.26 and 1.89 ℓ H_2S/min, 90% of the particles were below 107.1 µm, 64.4 µm and 34.1 µm, respectively, suggesting a higher tendency towards particle aggregation at lower H_2S flow-rates.

A somewhat higher percentage of residue was generated in the process, approximately 0.43 kg for every 1.0 kg CaS processed. The anhydrite, quartz and hydroxyapatite present in the CaS feed material were probably components of the residue, although this was not studied further. Full characterization of the residue in terms of the mineral and elemental composition is required. Unless specific uses can be identified for this residue, it will be classified as an industrial solid waste and would require special attention for its disposal and management.

Carbonation of $Ca(HS)_2$ solution for $CaCO_3$ production

Polymorphic transition of vaterite to calcite

$CaCO_3$ exists as three anhydrous crystalline polymorphs (calcite, aragonite, vaterite), two hydrated metastable forms (monohydrocalcite and calcium carbonate hexahydrate), and an unstable amorphous calcium carbonate (ACC) phase. Hydrated and amorphous forms are generally unstable and show a tendency toward transformation into one of the crystalline polymorphs unless it is stabilized by specific additives (Bots et al. 2012; Meldrum 2003).

The Ca-rich filtrate (462 mmol/ℓ as Ca and pH 9.74) generated by CaS dissolution of a 4% CaS slurry using H_2S gas, was subjected to gaseous CO_2 at a flow-rate of 1.12 ℓ/min to produce high-purity $CaCO_3$. Figure 5.15 shows the reaction dynamics (expressed as changes in solution pH and conductivity with time). When adding CO_2 (time = 0 min), the pH dropped sharply from 9.74 to 7.90 within a short period of time (~ 2 min), after which it continued decreasing more gradually down to approximately 6.47 after 33 min, before stabilizing at about 6.2. The solution conductivity decreased at a constant rate from 47.9 mS/cm down to 3.18 mS/cm during the first 33 min of reaction time before stabilising at 1.88 mS/cm. The carbonation reaction was complete in approximately 33 min (as indicated by the levelling off of the drop in the pH and solution conductivity).

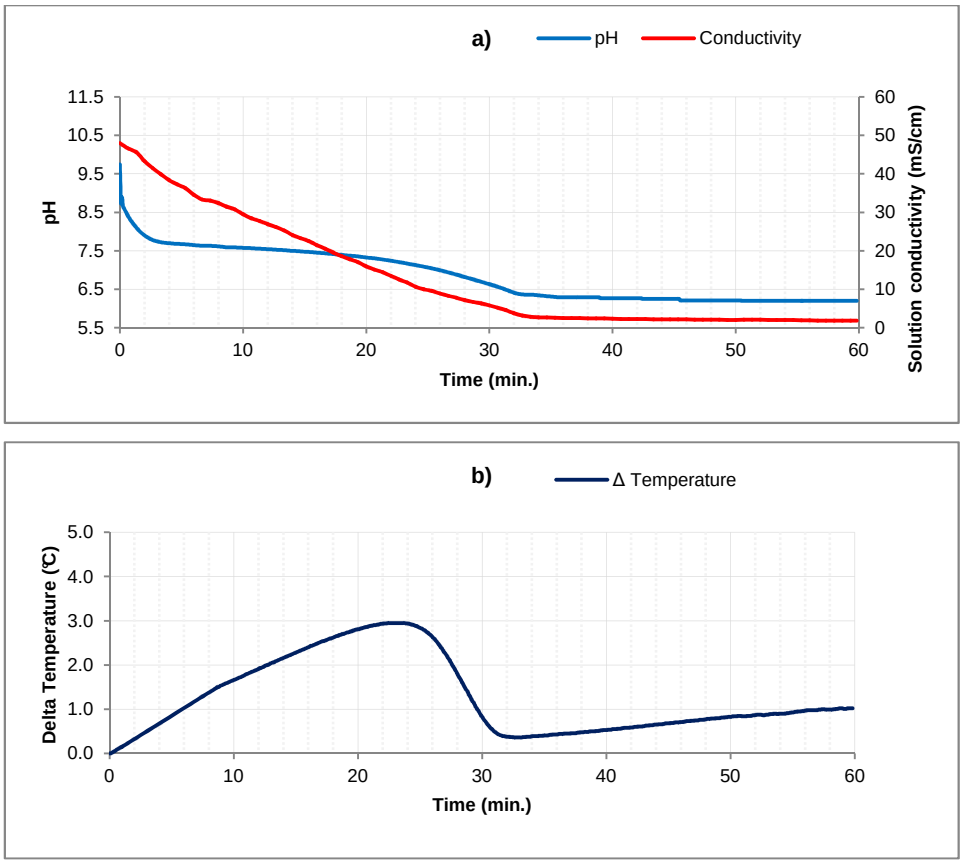

Figure 5.15 pH and solution conductivity profiles (a) and delta temperature (b) profiles with time during the carbonation of $Ca(HS)_2$ solution. (Initial Ca: 462 mmol /ℓ as Ca; initial pH: 9.74; stirring rate: 700 min^{-1}; gas flow-rate: 1.12 ℓ CO_2/min)

The mineral composition, particle size analysis and morphology of the solids at completion of the carbonation reaction are given in Table 5.6 and Figures 5.16.

Table 5.6 Experimental conditions and semi-quantitative XRD analysis (mass%) and particle size analysis of the high-grade $CaCO_3$ product.

$Ca(HS)_2$ carbonation : production of high-grade $CaCO_3$			
Experimental conditions	Sample ID		M69
	Volume	mℓ	3000
	Initial pH		9.74
	Initial calcium	mmol/ℓ	462
	Initial temperature	°C	19.34
	Gas flow-rate	ℓ CO_2/min	1.12
	Stirring	min^{-1}	700
Mineral composition	Calcite	mass%	97.28
	Quartz	mass%	0.53
	Sulphur	mass%	2.18
Particle size analysis		Mode size (µm)	24.5
		D10 (µm)	13.2
		D50 (µm)	24.6
		D90 (µm)	42.1
Actual yield		g	70.6

Figure 5.16 depicts the SEM micrographs of the solids recovered at various time intervals during the carbonation of a $Ca(HS)_2$ solution for the production of $CaCO_3$. SEM images of the solids formed revealed the presence of both vaterite and calcite (Figures 5.16 (a)-(c)). After 10 min of reaction time (Figure 5.16 (a)), vaterite particles of various shapes and sizes were observed together with some single, rhombohedral calcite particles. By the time the reaction had progressed for 20 min, only spherical vaterite aggregates with no irregular shapes were visible together with some larger calcite interpenetrated rhombi (Figure 5.16 (b)). At 30 min, the proportion of vaterite had decreased and only individual nanoparticulate subunits of vaterite crystals were present with even bigger calcite particles (Figure 5.16 (c)). Calcite was the major crystalline phase present in the second half of the carbonation experiment (Figure 5.16 (d) to (f), time 40 to 60 min).

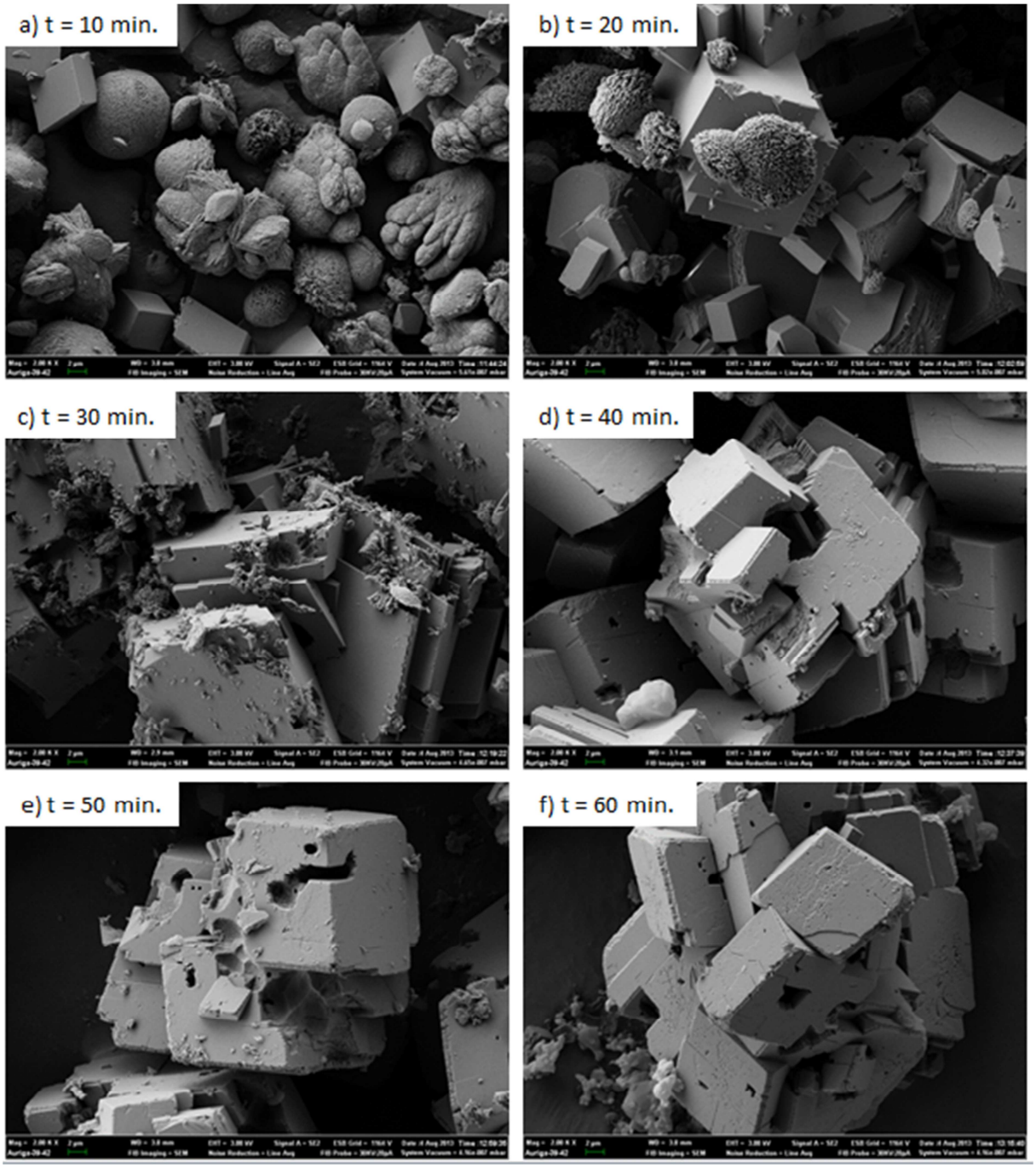

Figure 5.16 Scanning electron micrographs (2000 × magnification) of the solid phase recorded after a) 10 min, b) 20 min, c) 30 min, d) 40 min, e) 50 min, and f) 60 min of reaction time. (Initial Ca: 462 mmol /ℓ as Ca; initial pH: 9.74; stirring rate: 700 min^{-1}; gas flow-rate: 1.12 ℓ CO_2/min)

During the carbonation reaction, the proportion of vaterite progressively decreased as the calcite crystals formed on the surfaces of the vaterite aggregates (Figure 5.17 (a)-(c)). This suggested that vaterite particles slowly dissolved to release calcium near their surfaces, which rapidly carbonated in solution and re-precipitated on the surfaces of the vaterite particles. The casts, visible on the final

calcite end product were most probably the result of the calcite forming and growing on the surface of the initial vaterite particles.

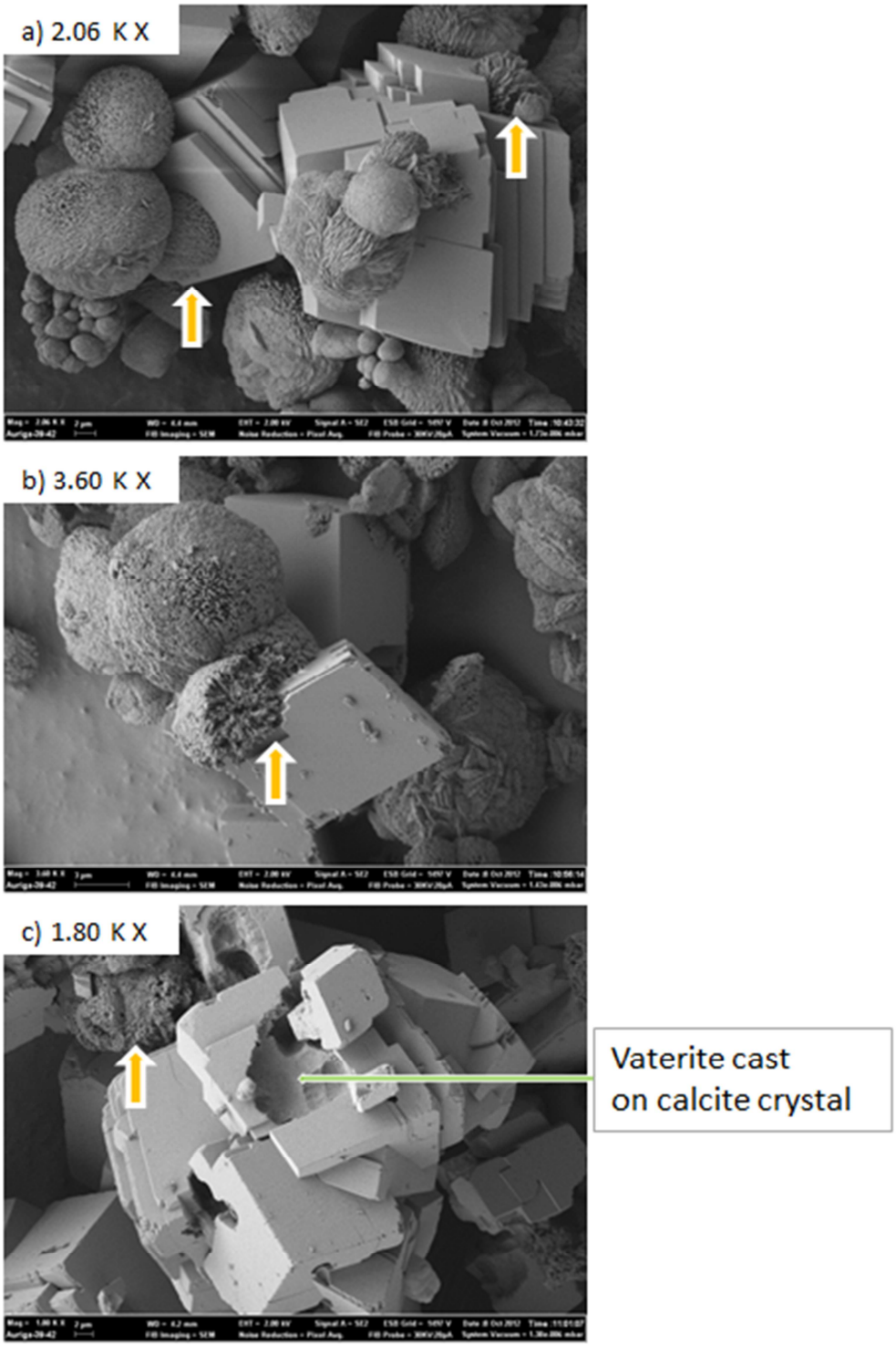

Figure 5.17 Scanning electron micrographs showing calcite crystals attached and grown on the surface of vaterite which led to the production of calcite crystals with vaterite casts

In the spontaneous precipitation of $CaCO_3$, ACC is known to occur first and because it is highly unstable (K_{sp} $10^{-6.40}$ at 25°C), it transforms almost immediately into a mixture of calcite and vaterite from an early stage (Rodriguez-Blanco et al. 2011). Vaterite is also in an intermediate and unstable phase of $CaCO_3$ (Pouget et al. 2010; Plummer & Busenberg 1982) and the higher solubility of vaterite (K_{sp} $10^{-7.913}$ at 25°C) compared to that of calcite (K_{sp} $10^{-8.480}$ at 25°C) in neutral to weak basic pH solutions resulted in the gradual transformation of vaterite into calcite (Rodriguez-Blanco et al. 2011). This transformation process has been explained by a number of research groups by the two-step recrystallization processes, namely, the dissolution of an unstable polymorph and the growth of a stable polymorph (Gopi et al. 2013; Sarkar & Mahapatra 2012; Wang et al. 2009; Nissenbaum et al. 2008). The transformation of vaterite into calcite only depends only on the supersaturation and not pH or temperatures in the range of 25 to 45°C (Spanos 1998)

Effect of process parameters on the reaction kinetics and $CaCO_3$ particle characteristics

The effect of the stirring mode (mechanical agitation *vs* ultrasound irradiation without mechanical stirring) at various CO_2 gas flow-rates on $Ca(HS)_2$ carbonation was also investigated.

The application of ultrasound during crystallization and precipitation processes is receiving increasing attention and ultrasound has been seen to promote the precipitation of different $CaCO_3$ polymorphs. The application of ultrasound to chemical reactions and the mechanism causing the sonochemical effects in liquids is the phenomenon of *acoustic cavitation* (Suslick et al. 1999). Ultrasonic irradiation is considered to lead to two types of prominent effects: 1) physical effects due to physical mixing (macrostreaming), and ii) chemical effects, due to cavitation leading to radical formation (microstreaming). The cavitation caused by ultrasonic activation has both physical and chemical effects.

Ultrasonic energy consists of mechanical vibrations occurring above the upper frequency limit of human audibility, generally accepted to be about 20 kHz. The use of ultrasound in chemical processes consists in applying sound waves in the range of 16–100 kHz (Luque de Castro & Priego-Capote 2007). Power is delivered to a solution by inducing cavitation, that is, the formation of small cavities or micro-bubbles that grow and collapse rapidly. The collapsing micro-bubbles produce high local temperatures and pressures and high shear forces (Suslick et al. 1999).

The application of power ultrasound to crystallizing systems appears to offer significant potential for modifying and improving both chemical processes and products (Parvizian et al. 2011). It is generally accepted that the ultrasonic field influences the crystallization process by enhancing the primary nucleation and preventing agglomeration. Sonochemistry has previously been applied to the precipitation of calcium carbonate (Mihai et al. 2009; Mateescu et al. 2007).

Comparisons between the reaction rates (Figure 5.18 (a)), reaction times (Figure 5.18 (b)) and the calculated reaction rate (mmol/ℓ/min as Ca, Table 5.7) at various CO_2 gas flow-rates under mechanical agitation and ultrasound irradiation, are presented. Increasing the CO_2 flow-rate from 0.36 to 0.90 to 1.62 ℓ/min causes the reaction time to decrease from 25 to 19 to 15 min, respectively, under mechanical agitation.

Similarly, the reaction times under ultrasound irradiation and identical CO_2 flow-rates decreased from 26 to 19 to 16 min. However, at identical CO_2 flow-rates, the rate constant for the $Ca(HS)_2$ carbonation reactions under mechanical agitation and ultrasound irradiation were found to be very similar. At 0.36 ℓ CO_2/min, the rate was 22.4 under mechanical agitation, and 21.5 mmol/ℓ/min (as Ca) under ultrasound irradiation, at 0.90 ℓ CO_2/min, 29.0 and 29.8 mmol/ℓ/min (as Ca) and at 1.62 ℓ CO_2/min, 37.9 and 35.7 mmol/ℓ/min (as Ca), respectively. The application of ultrasound therefore did not enhance the overall rate of the reaction.

The results of this study were not in agreement with the results of Nishida (2004) who reported that ultrasound irradiation accelerated the precipitation rate of $CaCO_3$ and attributed it to enhanced mixing, especially macrostreaming. Although the same type of ultrasonic probe and parameters (tip size, reactor volume) were used in the two different studies, Nishida et al. (2004) used a calcium solution containing 1.2 mmol/ℓ (as Ca) wheras a Ca-rich solution containing 560 mmol/ℓ (as Ca) was used in this study. The reason for this difference in the reported results of the two studies could also be ascribed to the different reaction systems used; liquid-liquid (Nishida 2004) *versus* our liquid-gas system. In the liquid-liquid method, a solution containing 2.4 mmol/ℓ of calcium chloride and a second solution containing 6.4 mmol/ℓ sodium bicarbonate of which the pH was adjusted to 9.1, were mixed. The ultrasonic irradiation was started just after the preparation of the reaction solution (Nishida 2004) and the temperature was kept constant at 30°C. In the liquid-gas reation, ultrasoun irradiation was applied for 10 min on the $Ca(HS)_2$ filtrate before CO_2 gas was introduced and the temperature was not controlled.

In this study, as well as the study of Nishida (2004), mechanical mixing and ultrasound irradiation were used seperately. The combination of mechanical mixing and ultrasound irradiation could have yielded a different outcome if they had been used together. This was not investigated further in this study.

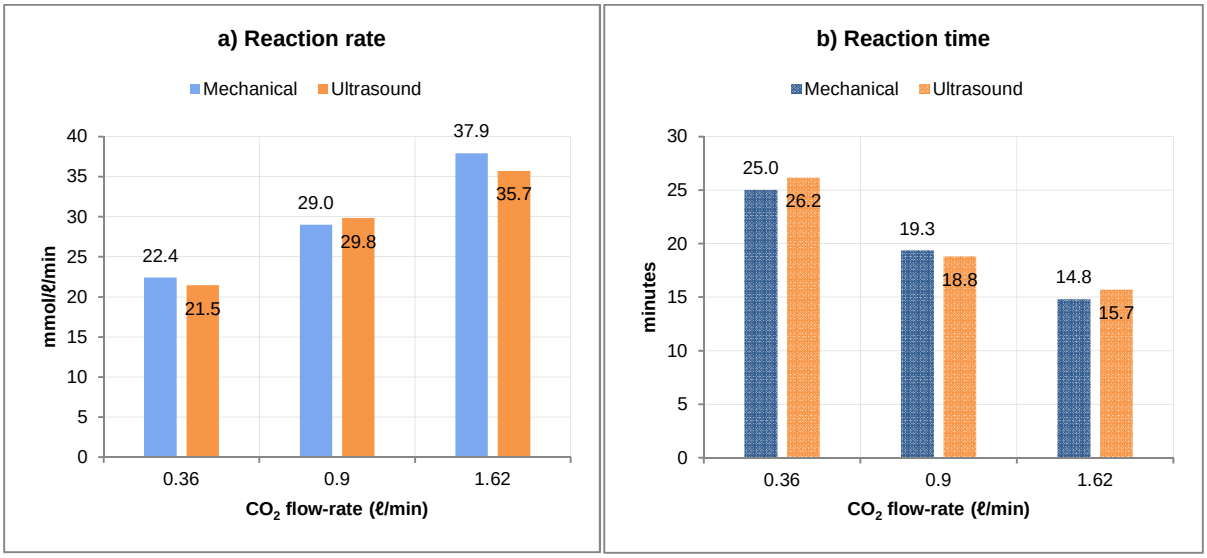

Figure 5.18 Comparison of the a) rate constants (mmol/ℓ/min as Ca) and b) reaction times of the $Ca(HS)_2$ carbonation reaction at various CO_2 flow-rates under mechanical agitation and ultrasound irradiation (Ultrasonic intensity: 460 W/cm^2; horn tip diameter: 3 mm; horn immersion depth: 10 mm)

Table 5.7 Reaction kinetics of the $Ca(HS)_2$ carbonation reaction at various CO_2 flow-rates under mechanical agitation (730 min^{-1}) and ultrasound irradiation (Ultrasonic intensity: 460 W/cm^2; horn tip diameter: 3 mm; horn immersion depth: 10 mm)

Stirring mode	**CO_2 flow (ℓ/min)**	**Initial reaction conditions**			**Reaction rates**			**Reaction time (min)**
		Soluble calcium (mmol/ℓ)	**pH**	**Temp. (°C)**	**Rate constant (mmol/ℓ/min as Ca)**	**Standard deviation (±)**	**R^2**	
Mechanical agitation	0.36	530	10.08	19.34	22.42	0.54	0.9155	25
	0.90	571	9.93	20.03	29.01	0.32	0.9894	19
	1.62	563	8.59	20.62	37.91	0.42	0.9889	15
Ultrasound irradiation	0.36	577	9.54	20.13	21.47	0.25	0.9882	26
	0.90	579	9.71	19.77	29.84	0.28	0.9924	19
	1.62	574	8.91	20.47	35.73	0.25	0.9955	16

The carbonation reaction or $CaCO_3$ precipitation step was also monitored by measuring the solution conductivity, pH and temperature changes with time at ambient temperature and under atmospheric pressure (all values logged at 5 second intervals). Figure 5.19 (a) shows the results obtained at various CO_2 flow-rates under mechanical agitation. The findings reported in Figure 5.19 (b) were obtained under ultrasound irradiation without mechanical stirring.

The high electrical conductivity values (> 55 mS/cm, Figures 5.19 (a i) and (b i)) of the solution after 10 min of mixing prior to the addition of CO_2 (time = 0 min) confirmed the high solubility of the $Ca(HS)_2$ solution. Immediately upon addition of CO_2, the pH dropped sharply from about 8.0 within the first two minutes of the reaction (Supplementary Information S5.4.2, p. 128), after which it continued decreasing more gradually down to approximately 6.4 (Figures 5.20 (a ii) and (b ii)). The gradual drop in solution pH exhibited two different slopes and the pH profiles were similar for both the mechanically agitated and ultrasound irradiated experimental runs at the various CO_2 gas flow-rates (Figures 5.19 (a ii) and (b ii)).

Similar profiles for the solution conductivities (steady decrease from about 55 mS/cm down to 3 mS/cm) were also observed for the two types of mixing (Figures 5.19 (a i) and (b i)). The decrease in the electrical conductivity was ascribed to the decrease of soluble ionic species in solution, namely the removal of soluble calcium due to $CaCO_3$ precipitation and sulphur due to H_2S gas stripping.

Although similar profiles for solution conductivity and pH were observed, a major difference in the temperature profiles between mechanically agitated runs were noted (initially slight increase followed by a gradual decrease) and ultrasound irradiation (continuous rise) (Figures 5.19 (a iii) and (b iii)). An inevitable consequence of using an ultrasonic horn is a rise in temperature of the bulk solution. Ultrasound irradiation causes mechanical vibration of the liquid, and when passing through the liquid medium, it produces heat by means of cavitation bubble implosion. It was noted that with ultrasound irradiation (Figure 5.19 (b iii)), the final temperature of the solutions were generally higher and this may have played a role in the nature of the precipitates obtained from the reactions, although it was previously demonstrated that this heat surplus did not affect the reaction kinetics of the carbonation process.

The results (Table 5.7 and Figure 5.20) showed that the increase in CO_2 flow-rates under the two types of mixing accelerated the calcium carbonation reaction. Neither of the modes of mixing showed positive effects on the reaction kinetics of the $Ca(HS)_2$ carbonation reaction.

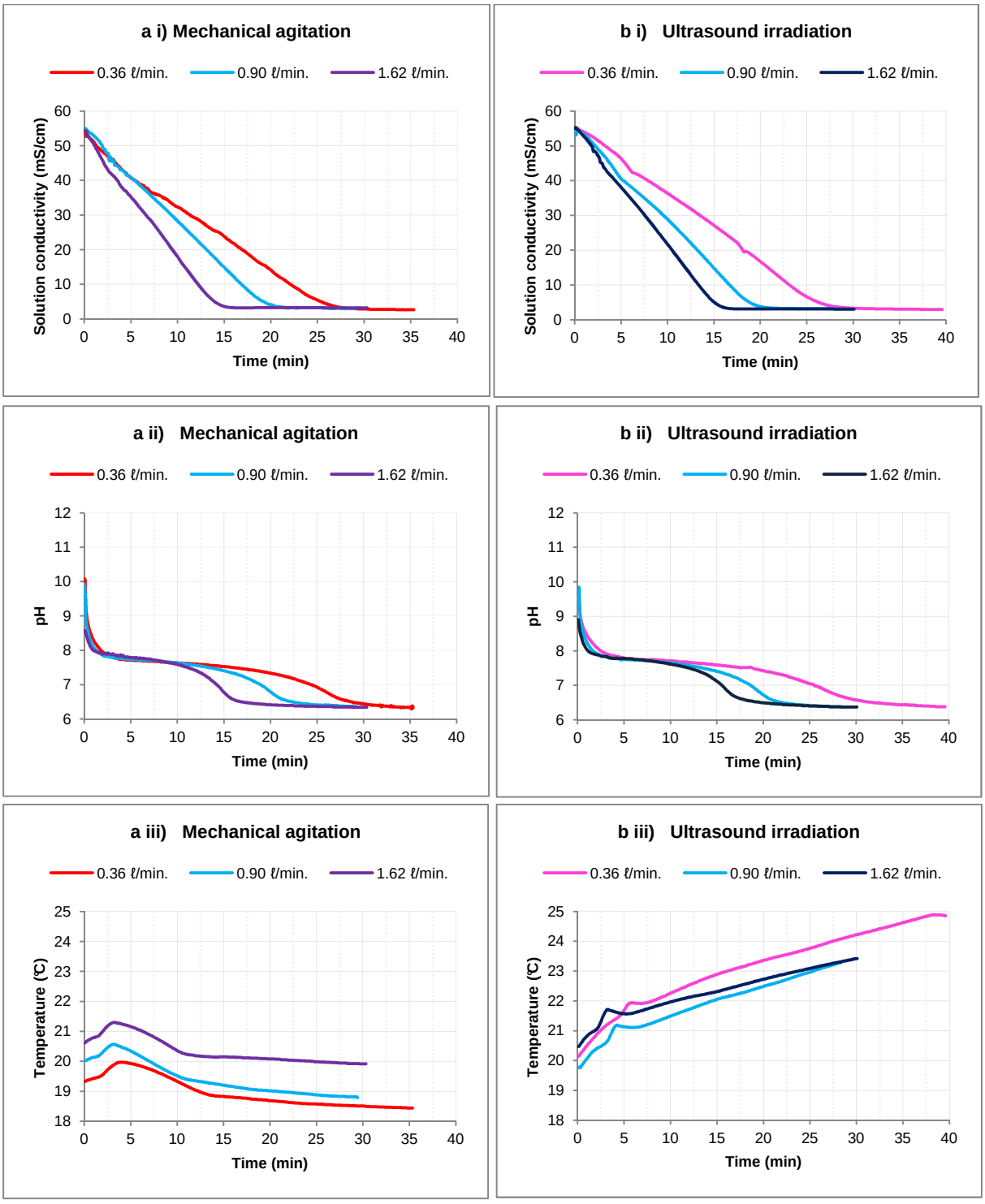

Figure 5.19 Effect of the CO_2 flow-rate combined with mechanical agitation (a) or ultrasound irradiation (b) on the (i) solution conductivity, (ii) pH and (iii) temperature with time (Ultrasonic intensity: 460 W/cm^2; horn tip diameter: 3 mm; horn immersion depth: 10 mm)

$CaCO_3$ characteristics

XRD, FTIR and SEM were employed to study the effect of CO_2 flow-rates and the effect of mixing mode on the crystal structure and polymorphs of the high-grade $CaCO_3$ particles produced. In this study only the calcite and vaterite polymorphs were formed. The formation of aragonite is generally associated with higher temperatures (> 50°C) and pressure (Liu et al. 2010) and all the experiments during this study were executed at ambient temperature and pressure.

The experimental conditions and mineral compositions of the $CaCO_3$ products generated under mechanical agitation and ultrasound irradiation at various CO_2 gas flow-rates are shown in Table 5.8. On the basis of their carbonate content (> 99 mass% as $CaCO_3$), the pure white products synthesised via the carbonation of $Ca(HS)_2$ solutions (Figure 5.20) were classified as high-grade $CaCO_3$, as previously suggested by Oates (1998). The small amount of quartz present in the high-grade $CaCO_3$ products is most probably microcrystalline quartz carried over from the starting material which had passed through the filter during the solids recovery step.

Table 5.8 Experimental conditions and semi-quantitative XRD analysis (mass%) of the high-grade $CaCO_3$ products generated at various CO_2 flow-rates under mechanical agitation and ultrasound irradiation

$Ca(HS)_2$ carbonation : production of high-grade $CaCO_3$								
Experimental conditions	Mixing mode		Mechanical agitation			Ultrasound irradiation		
	Sample ID		M103	M101	M95	M100	M102	M99
	Volume	mℓ	750	750	750	750	750	750
	Initial pH		10.1	9.9	8.6	9.5	9.7	8.9
	Initial calcium	mmol/ℓ	530	571	563	577	579	574
	Initial temperature	°C	19.34	20.03	20.62	20.13	19.77	20.47
	Gas flow-rate	ℓ CO_2/min	0.36	0.90	1.62	0.36	0.90	1.62
	Stirring	min^{-1}	730	730	730	-	-	-
Mineral composition	Calcite	mass%	99.22	78.16	71.12	79.05	23.02	14.04
	Vaterite	mass%	0.05	21.41	28.36	20.6	76.62	85.53
	Quartz	mass%	0.44	0.36	0.47	0.33	0.36	0.44
Particle size analysis		Mode size (µm)	36.8	24.3	24.5	14.2	16.3	14.1
		D10 (µm)	18.4	11.5	12.5	9.0	9.4	8.0
		D50 (µm)	36.0	24.4	25.3	17.1	16.8	13.9
		D90 (µm)	61.7	53.8	50.1	161.0	32.0	27.6
Actual yield		g	23.4	22.5	22.8	23.7	22.5	22.7

Figure 5.20 Photograph of the pure, white high-grade $CaCO_3$ product produced in the indirect CaS carbonation process

Although the $CaCO_3$ content of the high-grade $CaCO_3$ products generated under varying conditions of CO_2 rate and mixing (see 'actual yield' in Table 5.8) did not show significant variations in the total $CaCO_3$ content. The distribution ratio of polymorphs (calcite to vaterite) was greatly influenced by the CO_2 flow-rate as well as the mode of mixing.

Chakraborty et al. (1996) reported that the type of $CaCO_3$ crystalline form is dependent on the supersaturation level and ionic ratio of $[Ca^{2+}]/[CO_3^{2-}]$ in solution. When Ca-rich filtrates containing 560 mmol/ℓ (as Ca) were used for the carbonation reaction, mixtures of calcite and vaterite were formed. In comparison, when more dilute Ca-solutions (< 130 mmol/ℓ as Ca) were used, only calcite crystals were formed.

The variation in the proportions of calcite to vaterite is further illustrated in Figures 5.21 (a) and (b).

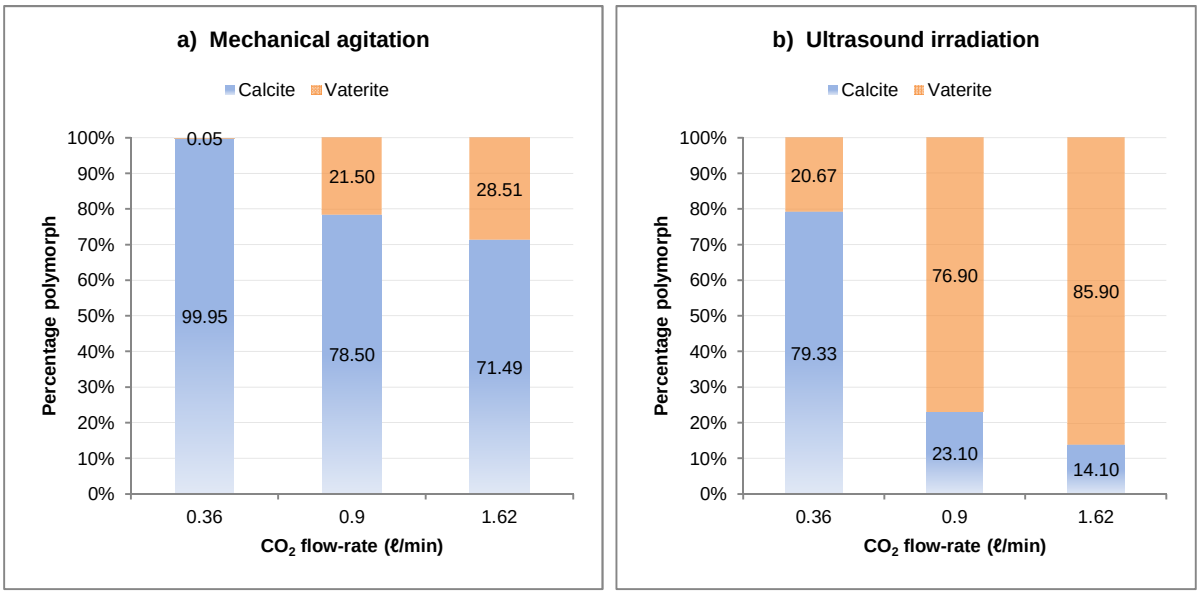

Figure 5.21 Variation of the $CaCO_3$ polymorph composition produced at different CO_2 flow-rates under a) mechanical agitation and b) ultrasound irradiation (Ultrasonic intensity: 460 W/cm^2; horn tip diameter: 3 mm; horn immersion depth: 10 mm)

The increase in CO_2 flow-rates led to a decrease in the calcite to vaterite ratio, regardless of the mode of mixing used. However, for every CO_2 flow-rate tested, much higher proportions of vaterite were produced when ultrasound irradiation was applied. A nearly pure calcite product (99.95 %) was obtained at low CO_2 flow-rate (0.36 ℓ/min) under mechanical agitation while a vaterite-calcite composite rich in vaterite (85.9 %) was produced at high CO_2 flow-rate (1.62 ℓ/min) and with ultrasound irradiation.

The structure of the high-grade $CaCO_3$ products was further investigated by FTIR. The different crystal forms of $CaCO_3$ show different bands in FTIR spectra, due to the difference in carbonate υ_2 deformation mode (out-of-plane deformation) and carbonate υ_4 band (in-plane deformation) (Xyla & Koutsoukos 1989). The characteristic transmittance peaks centred around 745(υ_4) and 873(υ_2) cm^{-1} correspond to the vibration modes of CO_3^{2-} in vaterite. For calcite, υ_4 shifts to 713 cm^{-1}, and the υ_2 position is similar with that of vaterite (Socrates 2001).

Infrared spectra of high-grade $CaCO_3$ crystals produced at different CO_2 flow-rates under mechanical agitation are presented in Figure 5.22. As shown in Figure 5.22 (a), at a low CO_2 flow-rate (0.36 ℓ/min) a single calcite phase was confirmed by the presence of the characteristic υ_2 band at 873 cm^{-1} and υ_4 band at 713 cm^{-1}. Increases in the CO_2 flow-rate from 0.36 to 0.90 ℓ/min (Figure 5.23 (b)) and to 1.62 ℓ/min (Figure 5.23 (c)) resulted in the appearance of a new peak located at 745 cm^{-1}, which is the fingerprint υ_4 deformation band of CO_3^{2-} in the vaterite form, indicating the presence of the vaterite phase. The characteristic transmittance peaks of calcite (713 cm^{-1}) and vaterite (745 cm^{-1}) substantiated the formation of a mixture of calcite and vaterite crystals at higher CO_2 flow-rates. It was also noted that the intensities of the peaks corresponding to calcite and vaterite became weaker and stronger, respectively, with higher CO_2 flow-rates, confirming the lower ratios of calcite to vaterite with increased CO_2 flow-rates.

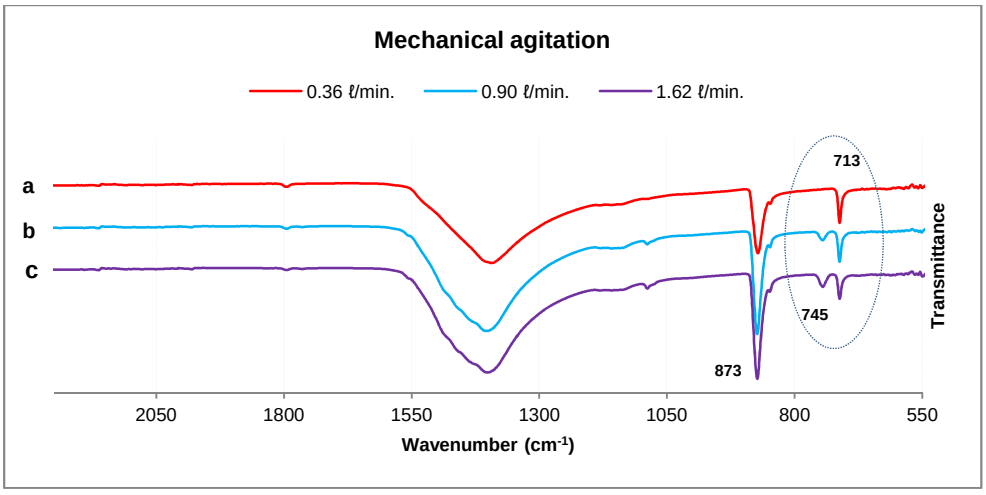

Figure 5.22 FTIR transmission spectra of $CaCO_3$ crystals produced under mechanical agitation at CO_2 flow-rates of a) 0.36 ℓ/min, b) 0.90 ℓ/min and c) 1.62 ℓ/min (Ca-rich solution containing ~560 mmol/ℓ as Ca)

Infrared spectra of high-grade $CaCO_3$ crystals produced at different CO_2 flow-rates under ultrasound irradiation are presented in Figure 5.23. The characteristic transmittance peaks of calcite (713 cm^{-1}) and vaterite (745 cm^{-1}), evident from Figure 5.23 (d)-(f) confirmed the presence of mixtures of calcite/vaterite crystals under ultrasound irradiation. Similar to the carbonation results under mechanical agitation, the intensities of the peaks corresponding to calcite and vaterite also became weaker and stronger, respectively, with increased CO_2 flow-rates, confirming lower ratios of calcite to vaterite formation at higher CO_2 flow-rates. The XRD results were therefore confirmed by FTIR under all experimental conditions tested.

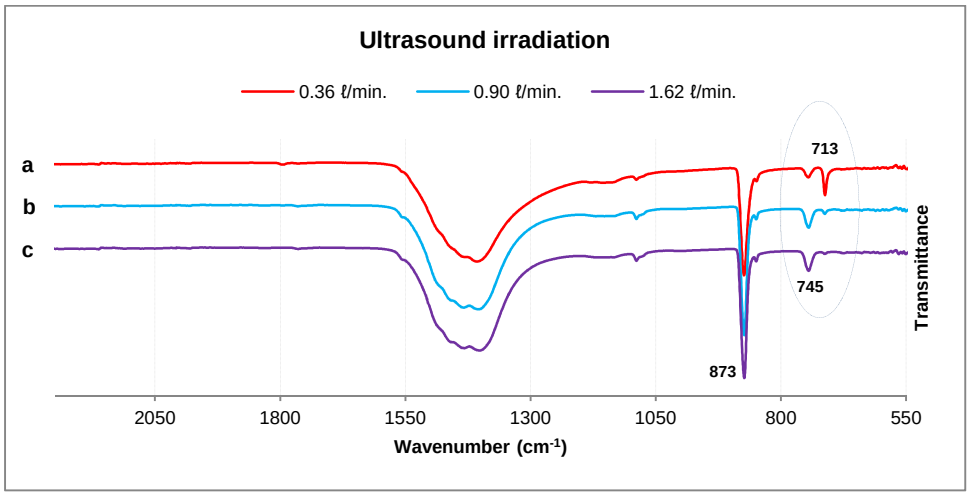

Figure 5.23 FTIR transmission spectra of $CaCO_3$ crystals produced under ultrasound irradiation at CO_2 flow-rates of a) 0.36 ℓ/min, b) 0.90 ℓ/min and c) 1.62 ℓ/min (Ca-rich solution containing ~560 mmol/ℓ as Ca). (Ultrasonic intensity: 460 W/cm^2; horn tip diameter: 3 mm; horn immersion depth: 10 mm)

The higher ratios of vaterite to calcite formed under ultrasound irradiation compared to mechanical agitation at identical CO_2 flow-rates were also confirmed by FTIR data. The characteristic transmittance peak of calcite (713 cm^{-1}) and the absence of the characteristic transmittance peak of vaterite (745 cm^{-1}) in Figure 2.24 (a i), confirmed the single calcite phase formed at the low CO_2 flow-rate of 0.36 ℓ/min under mechanical agitation. Under ultrasound irradiation and the same CO_2 flow-rate (Figure 5.24 (a ii)), the transmission peaks at 713 cm^{-1} and 745 cm^{-1} substantiated the formation of a mixture of calcite and vaterite crystals. Mixtures of calcite and vaterite were formed at higher CO_2 flow-rates (Figure 5.24 (b) and (c)). It was noted that the intensities of the peaks corresponding to vaterite were stronger and those for calcite, weaker under ultrasound irradiation

compared to mechanical agitation, indicating the formation of higher ratios of vaterite to calcite under ultrasound irradiation.

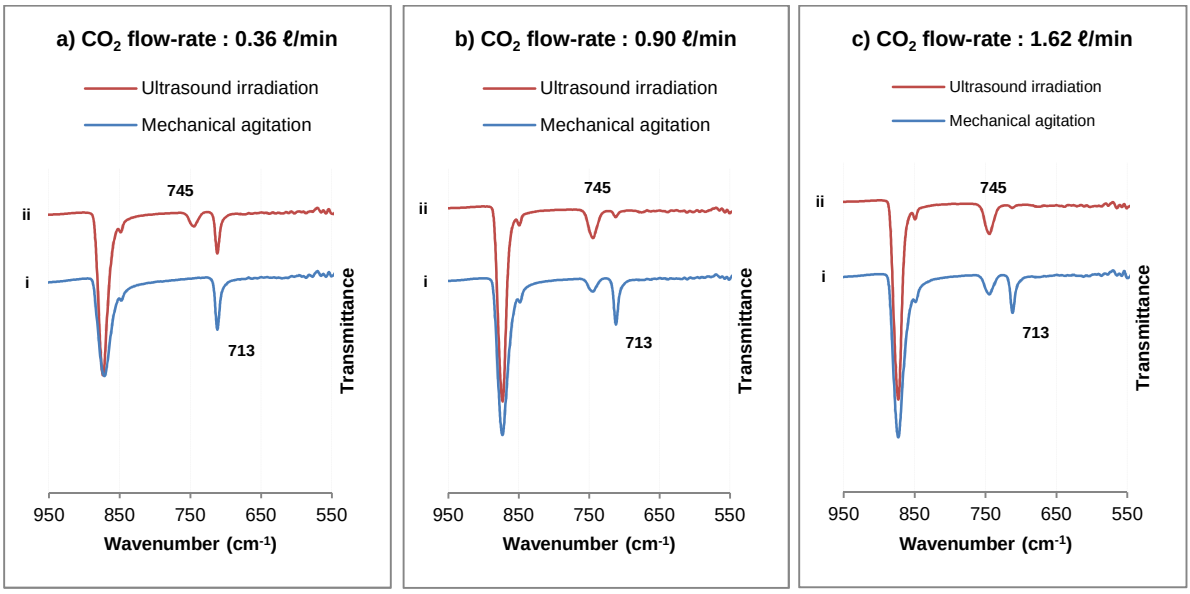

Figure 5.24 FTIR transmission spectra of $CaCO_3$ crystals produced at CO_2 flow-rates of a) 0.36 ℓ/min, b) 0.90 ℓ/min and c) 1.62 ℓ/min under mechanical agitation and ultrasound irradiation (Ca-rich solution containing ~560 mmol/ℓ as Ca) (Ultrasonic intensity: 460 W/cm^2; horn tip diameter: 3 mm; horn immersion depth: 10 mm)

Calcite usually crystallises as mono-crystalline well-faceted particles (Beck & Andreassen 2010). Vaterite particles, on the other hand, are usually poly-crystalline, exhibit a spherical shape, and are built up by smaller crystallites (Ibrahim et al. 2012). The SEM images (1000 × magnifications) of the $CaCO_3$ products generated are presented in Figure 5.25 (a)-(f) (images at lower magnification are available in Supplementary Information S5.5, pp. 129-130). Two co-occurring $CaCO_3$ phases (calcite and vaterite) can clearly be distinguished by their characteristic morphologies in Figure 5.25, which further supported the XRD and FTIR data. Calcite was recognised as the rhombohedral particles (Gehrke et al. 2005) and vaterite as the spherical crystallites.

The $CaCO_3$ produced under mechanical agitation (Figure 5.25 (a)-(c)) is well formed and the rhombohedral calcite crystals are clearly visible. The vaterite crystals produced under ultrasound irradiation are shown in Figure 5.25 (d)-(e).

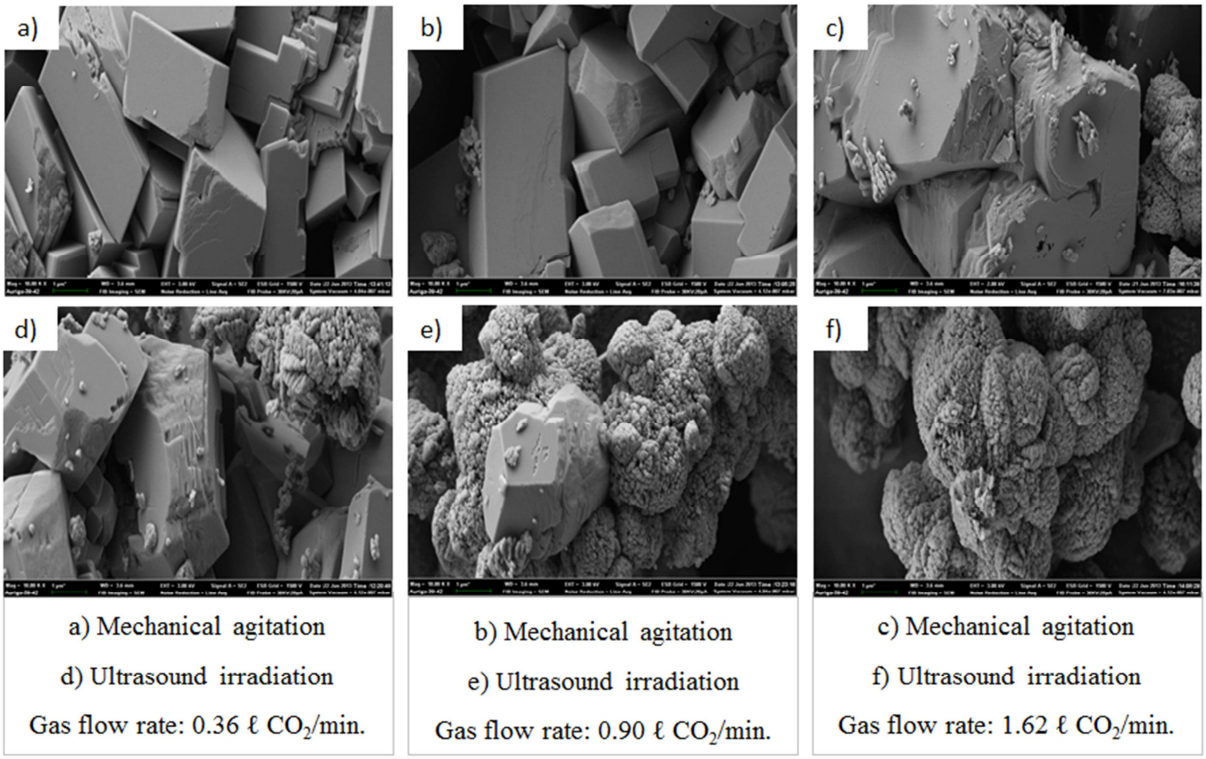

Figure 5.25 Scanning electron micrographs (1000 × magnification) of $CaCO_3$ crystals produced under mechanical agitation at CO_2 flow-rates of a) 0.36 ℓ/min, b) 0.90 ℓ/min and c) 1.62 ℓ/min and ultrasound irradiation at CO_2 flow-rates of d) 0.36 ℓ/min, e) 0.90 ℓ/min and f) 1.62 ℓ/min. (Ultrasonic intensity: 460 W/cm^2; horn tip diameter: 3 mm; horn immersion depth: 10 mm)

The results of this study differed from the results of Nishida (2004) who reported that the morphology of the precipitated $CaCO_3$ crystals, formed in their study, was unaffected by ultrasound irradiation. It should be noted that in their study they used a diluted Ca solution (1.2 mmol/ℓ) in a liquid-liquid reaction system whereas this study applied a liquid-gas carbonation process to a concentrated Ca solution (560 mmol/ℓ) which most probably accounted for the differences observed.

The $CaCO_3$ products were further characterised in terms of their specific surface area and density. The physical properties of the products generated at different CO_2 flow-rates under mechanical agitation and ultrasound irradiation are listed in Table 5.9. The distribution ratio of polymorphs (calcite to vaterite) had a major effect on the specific surface area and density of the products. The increase in CO_2 flow-rates led to a decrease in the calcite to vaterite ratio and an increase in the specific surface area of the particles. The measured specific surface area of the nearly pure calcite product (99.95 %) obtained at a low CO_2 flow-rate (0.36 ℓ/min) under mechanical agitation, was 0.26 m^2/g with a density of 2.71 g/cm^3. The specific surface area of the vaterite-calcite composite produced at a high CO_2

flow-rate (1.62 ℓ/min) under ultrasound irradiation with a 85.90 % vaterite content was much higher at 4.12 m^2/g. The density of this product, 2.62 g/cm^3, was lower than the typical density for calcite (2.72 g/cm^3) but higher than the typical density of vaterite (2.54 g/cm^3) (Plummer & Busenberg 1982).

Table 5.9 Physical properties of the high-grade $CaCO_3$ products produced at various CO_2 flow-rates under mechanical agitation and ultrasound irradiation. (Ca-rich solution containing ~560 mmol/ℓ as Ca)

Mixing mode	**CO_2 flow-rate (ℓ/min)**	**$CaCO_3$ polymorphs**		**BET surface area (m^2/g)**	**Density (g/cm^3)**
		Calcite (%)	**Vaterite (%)**		
Mechanical agitation	0.36	99.95	0.05	0.26 ± 0.010	2.71 ± 0.004
	0.90	78.50	21.50	1.47 ± 0.011	2.71 ± 0.003
	1.62	71.49	28.51	2.22 ± 0.011	2.70 ± 0.002
Ultrasound irradiation	0.36	79.33	20.67	2.01 ± 0.016	2.71 ± 0.004
	0.90	23.10	76.90	4.12 ± 0.006	2.62 ± 0.002
	1.62	14.10	85.90	4.33 ± 0.007	2.62 ± 0.003

5.3.3 Comparison of the indirect CaS carbonation process routes using CO_2 and H_2S gas for CaS dissolution

Two process configurations for the production of high-purity $CaCO_3$ from CaS via indirect mineral carbonation were studied at ambient temperature and pressure. First, CO_2 gas was used to induce CaS dissolution and generated a Ca-rich solution, whilst the second configuration made use of H_2S gas. In the second step of both the process routes, the particulate-free, Ca-rich solution was used to produce $CaCO_3$ of high purity. A summary of the characteristics of the solid products produced is given in Table 5.10.

Table 5.10 Comparison of the all solids characteristics produced via an indirect CaS carbonation process routes using CO_2 and H_2S gas for CaS dissolution.

	CO_2-gas route		**H_2S-gas route**			
Solid	Low-grade $CaCO_3$	High-grade $CaCO_3$	Residue	High-grade $CaCO_3$		
Reaction	CaS dissolution	$Ca(HS)_2$ carbonation	CaS dissolution	$Ca(HS)_2$ carbonation		
Reactor configuration	CSTR	CSTR	CSTR	CSTR	Glass beaker	Glass beaker
Mode of mixing	Overhead stirrer	Overhead stirrer	Overhead stirrer	Overhead stirrer	Magnetic stirrer	Ultrasonic irradiation
Actual mass (g/100g calcine)	90.6 ± 7.6	18.3 ± 5.3	43.1 ± 1.6	46.1 ± 1.6	45.8 ± 0.9	45.9 ± 1.3
$CaCO_3$ (mass%)	86.3 ± 4.8	99.4 ± 0.5	-	99.5 ± 0.03	99.4 ± 0.2	99.5 ± 0.04
Colour	Greyish-white	Pure white	Dark grey	Pure white	Pure white	Pure white
Mineral phase (Polymorph)	-	Calcite	Various structures	Calcite	Mixture of calcite and vaterite	Mixture of calcite and vaterite
Geo. Mean size (µm)	-	31.85 ± 1.59	15.3 ± 3.0	22.5 ± 2.0	25.4 ± 1.7	22.5 ± 2.0
[1]BET surface area (m^2/g)	-	1.19 to 1.95	-	-	0.26 to 0.22	2.01 to 4.33
Density (g/m^3)	-	2.72 ± 0.004	-	-	2.71± 0.04	2.62 ± 0.003

[1] Depends on the CO_2 flow rate during the carbonation reaction

5.4 Conclusion

The indirect calcium sulphide carbonation process, with two different process configurations, was studied. First, CO_2 gas was used for CaS dissolution in the first step of the process and the results showed that calcium carbonation and the subsequent precipitation of $CaCO_3$ took place concurrently with the CaS dissolution step, which resulted in the formation of a low-grade $CaCO_3$ product. After filtration of the leaching solutions, $CaCO_3$ of a higher level of purity (> 99% as $CaCO_3$) was produced. The high-grade $CaCO_3$ consisted of a single calcite phase (regardless of stirring rate or CO_2 flow-rate) and the morphology showed characteristic interpenetrated rhombohedral cubes of calcite. The particles produced at higher CO_2 flow-rates showed crystals with smoother surfaces, sharper edges and lower total surface area compared to products produced at lower CO_2 flow-rates.

In another process configuration, H_2S gas was used to induce CaS dissolution and a residue (low in calcium) was generated in the first step and a high-purity $CaCO_3$ (> 99% as $CacO_3$) in the second step. The process parameter studied in the CaS dissolution step was H_2S gas flow-rate. In the calcium carbonation reaction, the parameters were CO_2 flow-rate and mode of mixing i.e. mechanical agitation *versus* ultrasound irradiation.

Increasing the H_2S flow-rate succeeded in increasing the kinetics of the CaS dissolution and was shown to have little influence on the mineral composition of the residues generated.

Increasing the CO_2 flow-rate during the second step of the process increased the kinetics of the $CaCO_3$ precipitation/H_2S stripping reactions under both mechanical agitation and ultrasound irradiation. However, the nature of the $CaCO_3$ products in terms of the $CaCO_3$ polymorph ratios (vaterite to calcite) was affected. Mixtures of calcite and vaterite were produced and while the reaction was more rapid with higher flow-rates, the ratio of vaterite to calcite was also higher. Also, under ultrasound irradiation the amount of vaterite formed was higher and therefore also the polymorph ratios of $CaCO_3$, compared to mechanical agitation. The higher the ratio of vaterite in the vaterite-calcite composite samples, the higher the measured specific surface area and the lower the density of the product.

High-purity $CaCO_3$, for possible application in various industries, has been successfully produced *via* the indirect CaS carbonation process.

References

Beck, R. and Andreassen, J.P., 2010. Spherulitic growth of calcium carbonate. *Crystal Growth and Design*, 10(7), 2934-2947.

Bots, P., Benning, L.G., Rodriguez-Blanco, J., Roncal-Herrero, T. and Shaw, S., 2012. Mechanistic insights into the crystallization of amorphous calcium carbonate (ACC). *Crystal Growth and Design*, 12(7), 3806-3814.

Brecevic, L. and Nielsen, A.E., 1989. Solubility of amorphous calcium carbonate. *Journal of Crystal Growth*, 98(3), 504-510.

Chakraborty, D. and Bhatia, S.K., 1996. Formation and aggregation of polymorphs in continuous precipitation. 2. Kinetics of $CaCO_3$ precipitation. *Industrial and Engineering Chemistry Research*, 35(6), 1995-2006.

Dalas, E., 2001. Effect of ultrasonic field on calcium carbonate scale formation. *Journal of Crystal Growth*, 222(1-2), 287-292.

Eloneva, S., Teir, S., Revitzer, H., Salminen, J., Said, A., Fogelholm, C.J. and Zevenhoven, R., 2009. Reduction of CO_2 Emissions from steel plants by using steelmaking slags for production of marketable calcium carbonate. *Steel Research International*, 80(6), 415-421.

Gehrke, N., Cölfen, H., Pinna, N., Antonietti, M. and Nassif, N., 2005. Superstructures of calcium carbonate crystals by oriented attachment. *Crystal Growth and Design*, 5(4), 1317-1319.

Gopi, S., Subramanian, V.K. and Palanisamy, K., 2013. Aragonite-calcite-vaterite: A temperature influenced sequential polymorphic transformation of $CaCO_3$ in the presence of DTPA. *Materials Research Bulletin*, 48(5), 1906-1912.

Ibrahim, A.R., Vuningoma, J.B., Hu, X., Gong, Y., Hua, D., Hong, Y., Wang, H. and Li, J., 2012. High-pressure gas-solid carbonation route coupled with a solid ionic liquid for rapid synthesis of rhombohedral calcite. *Journal of Supercritical Fluids*, 72, 78-83.

Kim, W.S., Hirasawa, I. and Kim, W.S., 2004. Polymorphic change of calcium carbonate during reaction crystallization in a batch reactor. *Industrial and Engineering Chemistry Research*, 43(11), 2650-2657.

Kralj, D., Brecevic, L. and Kontrec, J., 1997. Vaterite growth and dissolution in aqueous solution III. Kinetics of transformation. *Journal of Crystal Growth*, 177(3-4), 248-257.

Liu, F., Gao, Y., Zhao, S., Shen, Q., Su, Y. and Wang, D., 2010. Biomimetic fabrication of pseudohexagonal aragonite tablets through a temperature-varying approach. *Chemical Communications*, 46(25), 4607-4609.

Lu, W.J., Guo, J.W., Cui, W.H. and Chen, H.H., 2009. Advances in production of precipitated calcium carbonate through CO_2 mineral sequestration by steel slag in acetic acid. *Modern Chemical Industry*, 29(2), 15-18.

Luque de Castro, M.D. and Priego-Capote, F., 2007. Ultrasound-assisted crystallization (sonocrystallization). *Ultrasonics sonochemistry*, 14(6), 717-724.

Ma, Y. and Feng, Q., 2011. Alginate hydrogel-mediated crystallization of calcium carbonate. *Journal of Solid State Chemistry*, 184(5), 1008-1015.

Maree, J.P., 2005. *Conversion of sulphur-containing waste material into a sulphur-containing product.* Australia: AU 2005201759 patent. Available from: <http://ip.com/patfam/en/35455786>.

Mateescu, C.D., Mocioi, M., Sarbu, C., Branzoi, F. and Chilibon, I., 2007. Morphology of $CaCO_3$ precipitated in ultrasonic field, *6th International Conference of the Balkan Physical Union*, 22 - 26 August 2007, pp626.

Mbhele, N.R., Van der Merwe, W., Maree, J.P. and Theron, D., 2009. Recovery of sulphur from waste gypsum, *Abstracts of the International Mine Water Conference,* 19-23 October 2009, pp. 622-630.

Meldrum, F.C., 2003. Calcium carbonate in biomineralisation and biomimetic chemistry. *International Materials Reviews,* 48(3), 187-224.

Menahem, T. and Mastai, Y., 2008. Controlled crystallization of calcium carbonate superstructures in macroemulsions. *Journal of Crystal Growth,* 310(15), 3552-3556.

Mihai, M., Turtoi, D., Isopescu, R., Mateescu, C. and Chiubon, I., 2009. Calcium carbonate synthesis in ultrasonic field. *Revista de Chimie,* 60(6), 626-631.

Nishida, I., 2004. Precipitation of calcium carbonate by ultrasonic irradiation. *Ultrasonics sonochemistry,* 11(6), 423-428.

Nissenbaum, J., Stipp, S.L.S. and Johnnson, A., 2008. Transformation of calcium carbonate polymorphs: Preliminary results. *Mineralogical Magazine,* 72(1), 473-476.

Oates, J.A.H., 1998. *Lime and limestone: Chemistry and technology, production and uses:* Weinheim: Wiley-VCH Verlag GmbH, Germany.

Parvizian, F., Rahimi, M. and Faryadi, M., 2011. Macro- and micromixing in a novel sonochemical reactor using high frequency ultrasound. *Chemical Engineering and Processing: Process Intensification,* 50(8), 732-740.

Plummer, L.N. and Busenberg, E., 1982. The solubilities of calcite, aragonite and vaterite in CO_2-H_2O solutions between 0 and 90°C, and an evaluation of the aqueous model for the system $CaCO_3$-CO_2-H_2O. *Geochimica et Cosmochimica Acta,* 46(6), 1011-1040.

Pouget, E.M., Bomans, P.H.H., Dey, A., Frederik, P.M., De With, G. and Sommerdijk, N.A.J.M., 2010. The development of morphology and structure in hexagonal vaterite. *Journal of the American Chemical Society,* 132(33), 11560-11565.

Rodriguez-Blanco, J.D., Shaw, S. and Benning, L.G., 2011. The kinetics and mechanisms of amorphous calcium carbonate (ACC) crystallization to calcite, via vaterite. *Nanoscale,* 3(1), 265-271.

Rodriguez-Blanco, J.D., Shaw, S., Bots, P., Roncal-Herrero, T. and Benning, L.G., 2012. The role of pH and Mg on the stability and crystallization of amorphous calcium carbonate. *Journal of Alloys and Compounds,* 536(Suppl.1), S477-S479.

Ruto, S., Maree, J.P., Zvinowanda, C.M., Louw, W.J. and Kolesnikov, A.V., 2011. Thermal studies on gypsum in a pilot-scale, rotary kiln, *Water in the South African Minerals Industry Conference,* 15-17 February 2011, The Southern African Institute of Mining and Metallurgy, The Southern African Institute of Mining and Metallurgy.

Said, A., Mattila, H., Järvinen, M. and Zevenhoven, R., 2013. Production of precipitated calcium carbonate (PCC) from steelmaking slag for fixation of CO_2. *Applied Energy,* 112, 765-771.

Santos, R.M., Ceulemans, P. and Van Gerven, T., 2012. Synthesis of pure aragonite by sonochemical mineral carbonation. *Chemical Engineering Research and Design,* 90(6), 715-725.

Sarkar, A. and Mahapatra, S., 2012. Mechanism of unusual polymorph transformations in calcium carbonate: Dissolution-recrystallization vs additive-mediated nucleation. *Journal of Chemical Sciences,* 124(6), 1399-1404.

Socrates, G., 2001. *Infrared and Raman characteristic group frequencies:* 3rd Edition. England: John Wiley & Sons Ltd.

Spanos, N. and Koutsoukos, P.G., 1998. The transformation of vaterite to calcite: effect of the conditions of the solutions in contact with the mineral phase. *Journal of Crystal Growth,* 191(4), 783-790.

Suslick, K.S., Didenko, Y., Fang, M.M., Hyeon, T., Kolbeck, K.J., McNamara III, W.B., Mdleleni, M.M. and Wong, M., 1999. Acoustic cavitation and its chemical consequences. *Philosophical Transactions of the Royal Society A: Mathematical, Physical and Engineering Sciences,* 357(1751), 335-353.

Teir, S., Eloneva, S. and Zevenhoven, R., 2005. Production of precipitated calcium carbonate from calcium silicates and carbon dioxide. *Energy Conversion and Management,* 46(18-19), 2954-2979.

Teir, S., Eloneva, S., Fogelholm, C. and Zevenhoven, R., 2007. Dissolution of steelmaking slags in acetic acid for precipitated calcium carbonate production. *Energy,* 32(4), 528-539.

Teir, S., Eloneva, S., Fogelholm, C. and Zevenhoven, R., 2006. Stability of calcium carbonate and magnesium carbonate in rainwater and nitric acid solutions. *Energy Conversion and Management,* 47(18-19), 3059-3068.

Wang, X., Kong, R., Pan, X., Xu, H., Xia, D., Shan, H. and Lu, J.R., 2009. Role of ovalbumin in the stabilization of metastable vaterite in calcium carbonate biomineralization. *Journal of Physical Chemistry B,* 113(26), 8975-8982.

Xu, X., Zhao, Y., Lai, Q. and Hao, Y., 2011. Effect of polyethylene glycol on phase and morphology of calcium carbonate. *Journal of Applied Polymer Science,* 119(1), 319-324.

Xyla, A.G. and Koutsoukos, P.G., 1989. Quantitative analysis of calcium carbonate polymorphs by infrared spectroscopy. *Journal of the Chemical Society, Faraday Transactions 1: Physical Chemistry in Condensed Phases,* 85(10), 3165-3172.

Supplementary Information to Chapter 5: The indirect CaS carbonation process.

S5.1. Calcine feed material

X-ray diffraction (XRD) results

The samples were prepared for XRD analysis using a back loading preparation method. The samples were analysed with a PANalytical X'Pert Pro powder diffractometer with X'Celerator detector and variable divergence- and fixed receiving slits with Fe filtered Co-Kα radiation. The phases were identified using X'Pert Highscore plus software. The relative phase amounts (mass%) were determined using the Rietveld method.

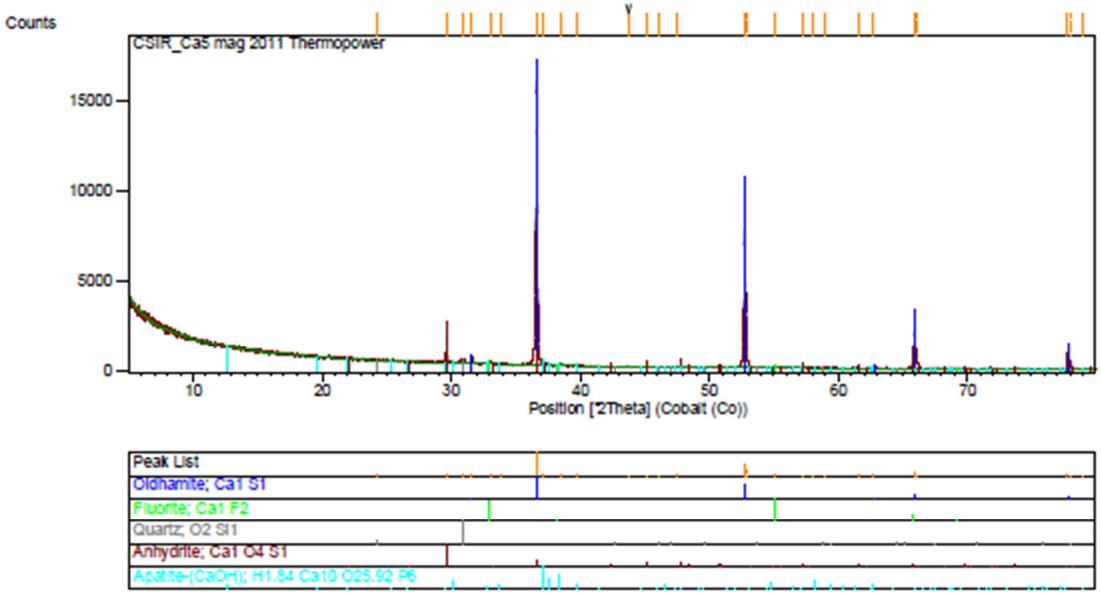

Figure S5.1.1 XRD diffractogram of the calcine feed material used during the indirect CaS carbonation process

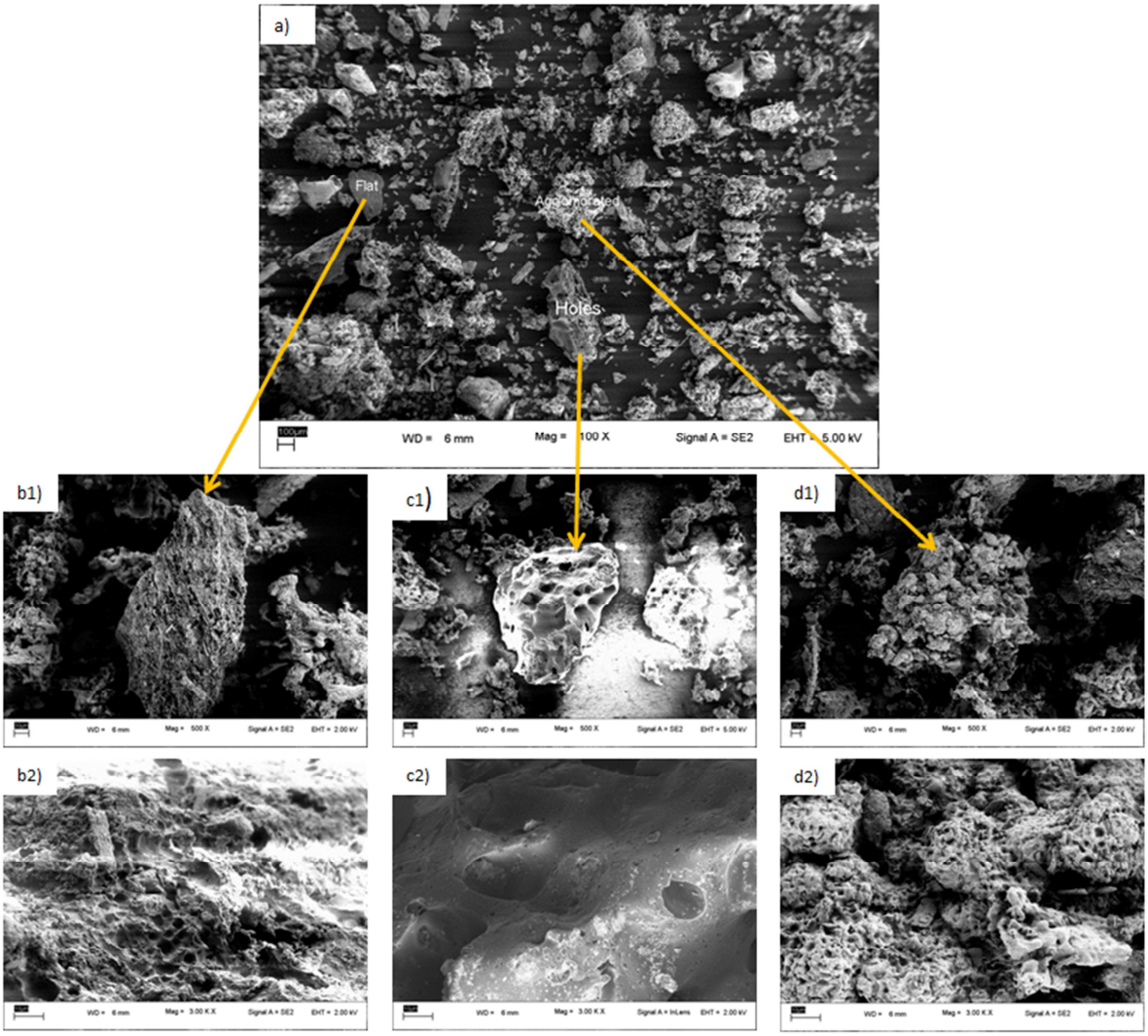

Figure S5.1.2 SEM micrographs of calcine feed material containing three different structures: b) Flat particles; c) particles with holes and d) agglomerates

S5.2. Effect of CO_2 flow-rate on the surface characteristics of the high-grade $CaCO_3$

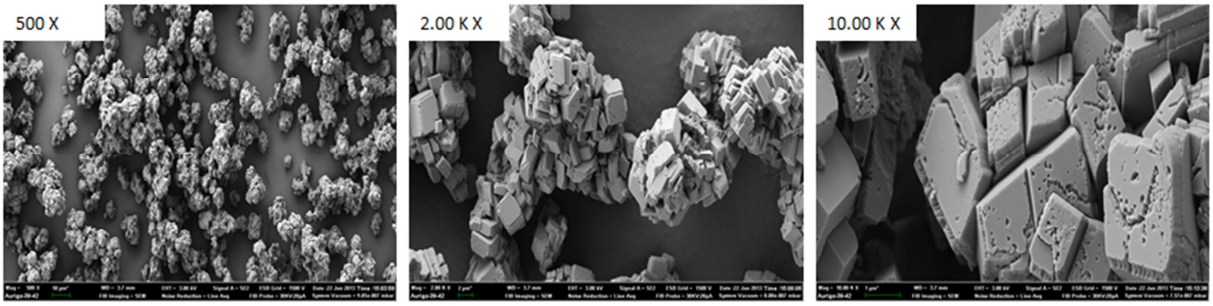

Figure S5.2.1 SEM micrographs of the high-purity $CaCO_3$ produced in the indirect carbonation process using CO_2 gas for CaS dissolution. (Ca-rich solution containing 22.5 g /ℓ as Ca; initial pH: 10.5; stirring rate: 580 min^{-1}; gas flow-rate: 0.44 ℓ CO_2/min; 3ℓ CSTR reactor)

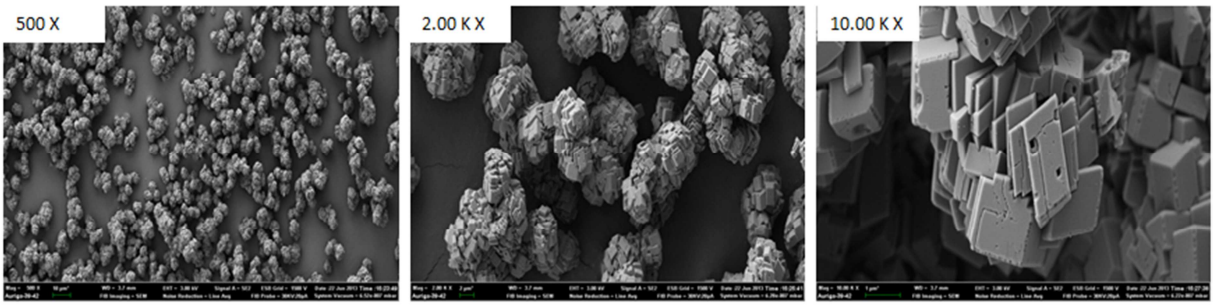

Figure S5.2. SEM micrographs of the high-purity $CaCO_3$ produced in the indirect carbonation process using CO_2 gas for CaS dissolution. (Ca-rich solution containing 22.5 g /ℓ as Ca; initial pH: 10.5; stirring rate: 580 min^{-1}; gas flow-rate: 1.90 ℓ CO_2/min; 3ℓ CSTR reactor)

S5.3. PSA of the residue produced at various H_2S gas flow-rates

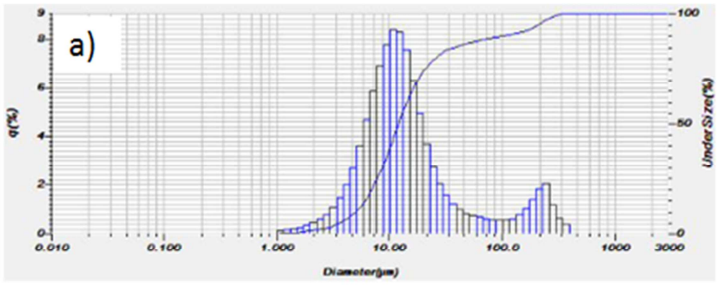

Median size : 12.1650 (μm)
Mean size : 35.2938 (μm)
Std. dev. : 65.0263 (μm)
Geo. mean size : 15.2767 (μm)
Geo. std. dev. : 3.0347 (μm)
Mode size : 10.8521 (μm)
Span : 8.3789 (μm)
Diameter on cumulative %
: 10.00(%) 5.1348 (μm)
: 50.00(%) 12.1650 (μm)
: 90.00(%) 107.0640 (μm)

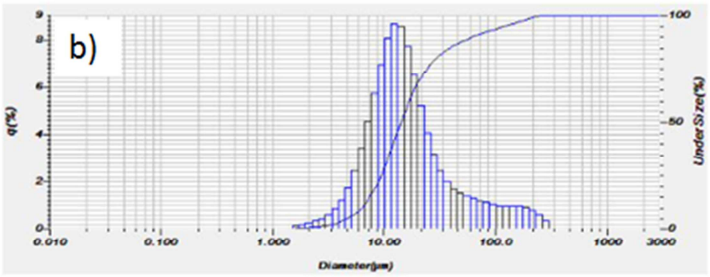

Median size : 14.3020 (μm)
Mean size : 28.4104 (μm)
Std. dev. : 41.9794 (μm)
Geo. mean size : 16.7276 (μm)
Geo. std. dev. : 2.4917 (μm)
Mode size : 12.4242 (μm)
Span : 4.0589 (μm)
Diameter on cumulative %
: 10.00(%) 6.3459 (μm)
: 50.00(%) 14.3020 (μm)
: 90.00(%) 64.3971 (μm)

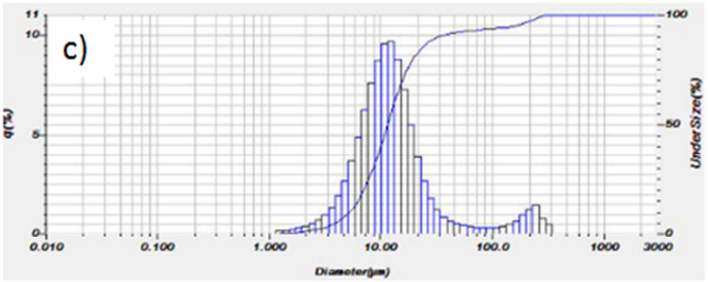

Median size : 11.6437 (μm)
Mean size : 26.3561 (μm)
Std. dev. : 52.0340 (μm)
Geo. mean size : 13.3003 (μm)
Geo. std. dev. : 2.5621 (μm)
Mode size : 12.3088 (μm)
Span : 2.4702 (μm)
Diameter on cumulative %
: 10.00(%) 5.3115 (μm)
: 50.00(%) 11.6437 (μm)
: 90.00(%) 34.0734 (μm)

Figure S5.3 Laser scattering particle size distribution analysis of the residues generated at various H_2S gas flow-rates: a) 0.96 ℓ/min, b) 1.26 ℓ/min and c) 1.89 ℓ/min in the CaS dissolution step. (CaS slurry containing 22.5 g /ℓ as Ca; initial pH: 11.8; stirring rate: 700 min^{-1})

S5.4 $Ca(HS)_2$ carbonation reaction (following CaS dissolution using $H_2S(g)$)

S5.4.1 Laser scattering particle size distribution analysis of the high-purity $CaCO_3$

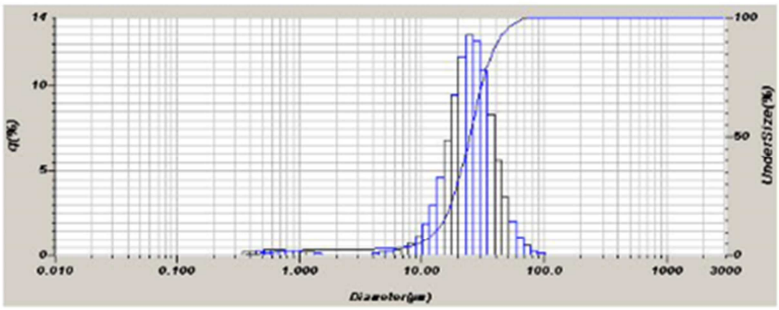

Median size : 24.6566 (μm)
Mean size : 26.3781 (μm)
Std dev. : 12.5098 (μm)
Geo. mean size : 22.5827 (μm)
Geo. std dev. : 2.0106 (μm)
Mode size : 24.5196 (μm)
Diameter on cumulative %
: (1) 10.00 %: 13.1604 (μm)
: (2) 30.00 %: 19.6548 (μm)
: (3) 40.00 %: 22.1347 (μm)
: (4) 50.00 %: 24.6566 (μm)
: (5) 60.00 %: 27.4192 (μm)
: (6) 70.00 %: 30.6381 (μm)
: (7) 80.00 %: 34.8770 (μm)
: (8) 90.00 %: 42.1084 (μm)
: (9) 95.00 %: 49.3418 (μm)

Figure S5.4.1 Laser scattering particle size distribution analysis of the high-purity $CaCO_3$ produced during the carbonation step. (Ca-rich solution containing 462 mmol/ℓ as Ca; initial pH: 9.47; stirring rate: 700 min^{-1}; gas flow-rate: 1.12 ℓ CO_2/min; 1ℓ CSTR reactor)

S5.4.2 Initial pH drop upon CO_2 addition to $Ca(HS)_2$ solution

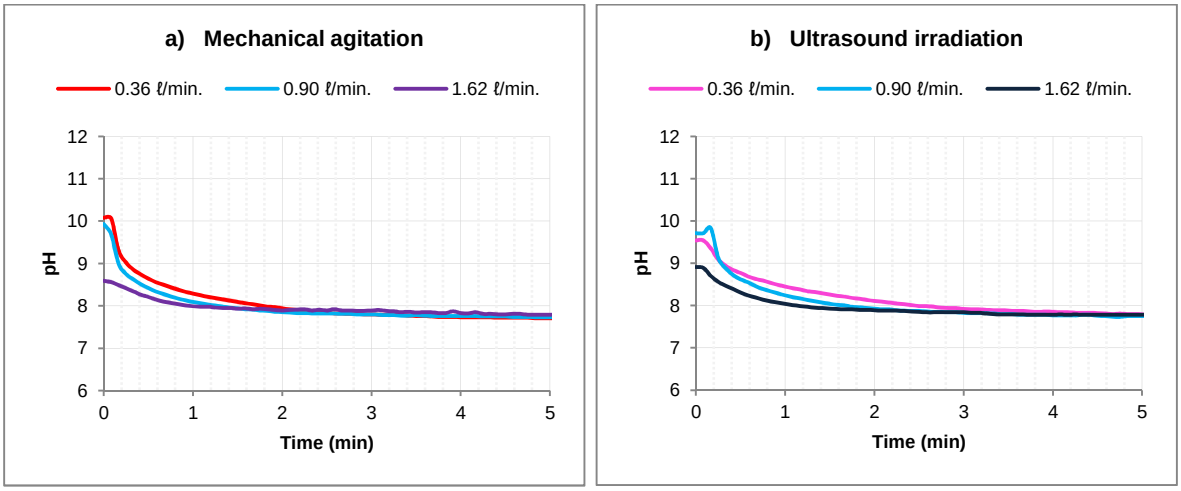

Figure S5.4.2 Initial drop in pH upon the addition of CO_2 gas to the $Ca(HS)_2$ solution with time under a) mechanical agitation and b) ultrasound irradiation (Ca-rich solution containing 560 mmol/ℓ as Ca)

S5.5 SEM micrographs at low magnification of $CaCO_3$ products produced at various CO_2 flow-rates under mechanical agitation and ultrasound irradiation.

S5.5.1 SEM micrographs at low magnification of $CaCO_3$ products produced at various CO_2 flow-rates under mechanical agitation

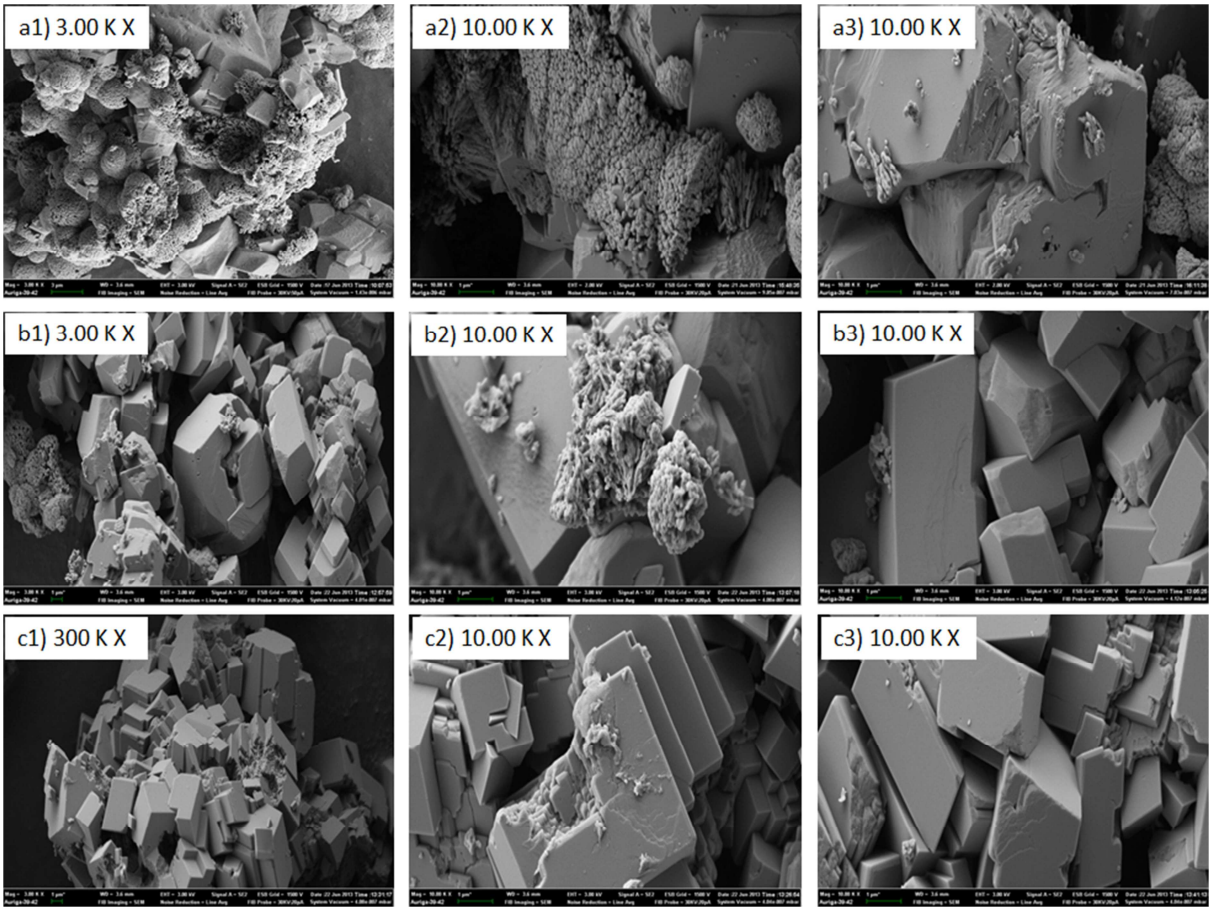

Figure S5.5.1 Scanning electron micrographs of $CaCO_3$ crystals produced under mechanical agitation at CO_2 flow-rates of a) 0.36 ℓ/min, b) 0.90 ℓ/min and c) 1.62 ℓ/min (Ca-rich solution containing 560 mmol/ℓ as Ca; stirring; 730 min^{-1})

S5.5.2 SEM micrographs at low magnification of $CaCO_3$ products produced at various CO_2 flow-rates under ultrasound irradiation

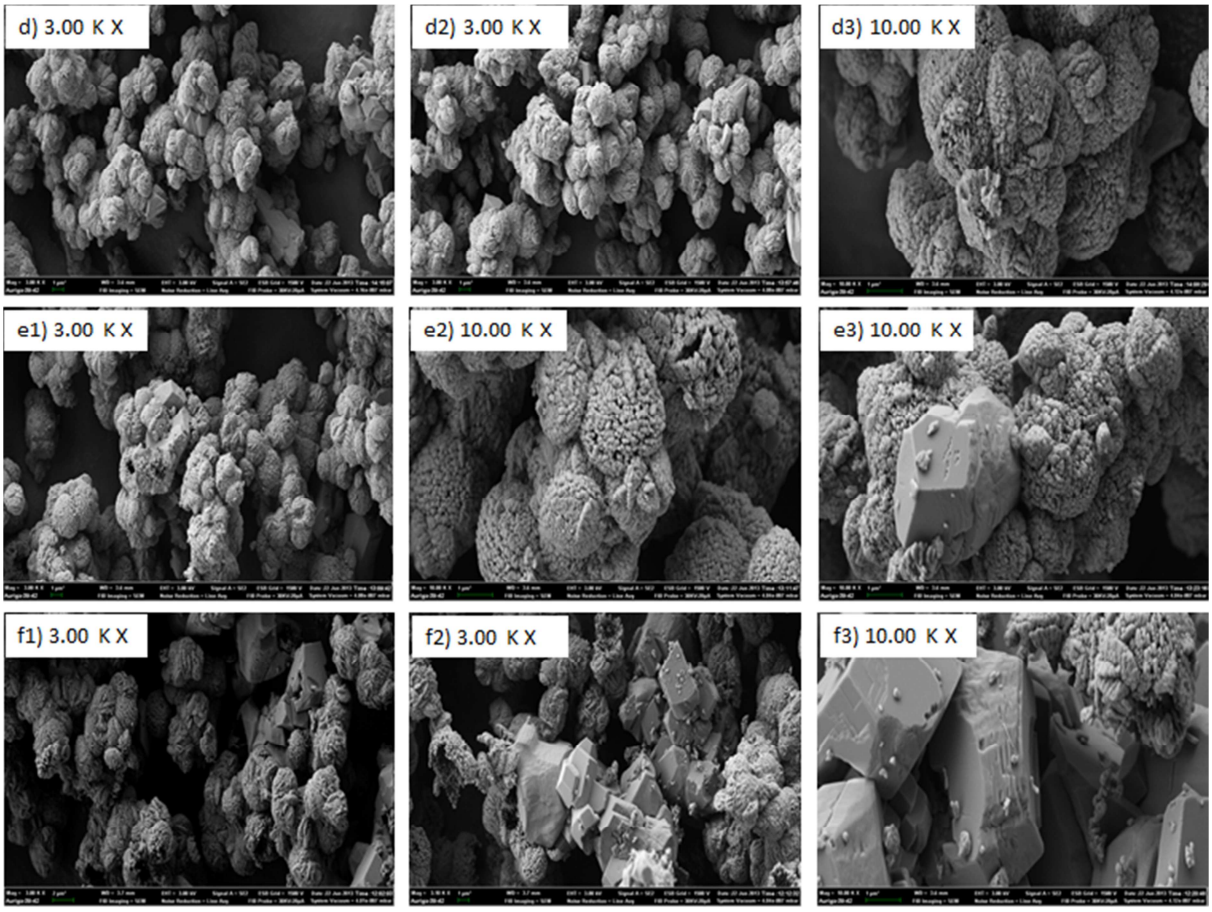

Figure S5.5.2 Scanning electron micrographs of $CaCO_3$ crystals produced under and ultrasound irradiation at CO_2 flow-rates of d) 0.36 ℓ/min, e) 0.90 ℓ/min and f) 1.62 ℓ/min (Ca-rich solution containing 560 mmol/ℓ as Ca)

S5.6 Particle size analysis of $CaCO_3$ products produced at various CO_2 flow-rates under mechanical agitation and ultrasound irradiation.

S5.6.1 Particle size analysis of $CaCO_3$ products produced at various CO_2 flow-rates under mechanical agitation

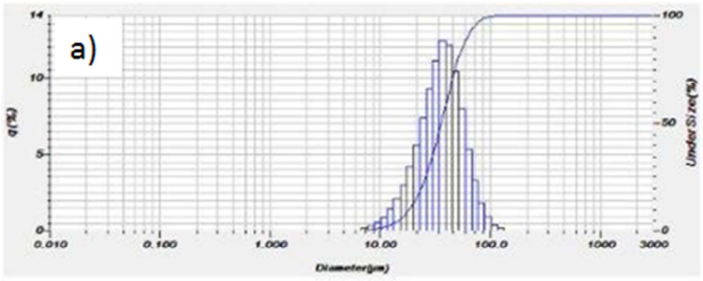

Median size : 35.9873 (μm)
Mean size : 38.5688 (μm)
Std. dev. : 17.6323 (μm)
Geo. mean size : 34.7223 (μm)
Geo. std. dev. : 1.6021 (μm)
Mode size : 36.8508 (μm)
Span : Off
Diameter on cumulative %
: 10.00(%) 18.4260 (μm)
: 50.00(%) 35.9873 (μm)
: 90.00(%) 61.7553 (μm)

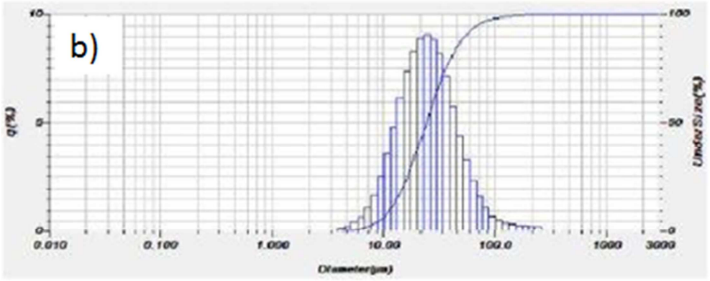

Median size : 24.3650 (μm)
Mean size : 30.7130 (μm)
Std. dev. : 25.4354 (μm)
Geo. mean size : 24.8184 (μm)
Geo. std. dev. : 1.8684 (μm)
Mode size : 24.2919 (μm)
Span : Off
Diameter on cumulative %
: 10.00(%) 11.4981 (μm)
: 50.00(%) 24.3650 (μm)
: 90.00(%) 53.8436 (μm)

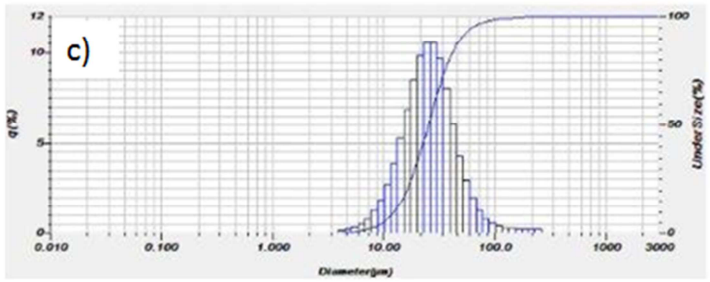

Median size : 25.3241 (μm)
Mean size : 30.4118 (μm)
Std. dev. : 23.4801 (μm)
Geo. mean size : 25.4001 (μm)
Geo. std. dev. : 1.773 (μm)
Mode size : 24.5217 (μm)
Span : Off
Diameter on cumulative %
: 10.00(%) 12.5255 (μm)
: 50.00(%) 25.3241 (μm)
: 90.00(%) 50.1011 (μm)

Figure S5.6.1 Scanning electron micrographs of $CaCO_3$ crystals produced under mechanical agitation at CO_2 flow-rates of a) 0.36 ℓ/min, b) 0.90 ℓ/min and c) 1.62 ℓ/min (Ca-rich solution containing 560 mmol/ℓ as Ca; stirring; 730 min^{-1})

S5.6.2 Particle size analysis of $CaCO_3$ products produced at various CO_2 flow-rates under ultrasound irradiation

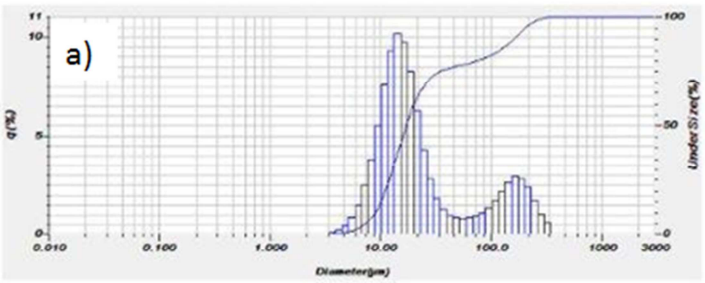

Median size : 17.0694 (μm)
Mean size : 47.9618 (μm)
Std. dev. : 66.5231 (μm)
Geo. mean size : 24.5713 (μm)
Geo. std. dev. : 2.8570 (μm)
Mode size : 14.2204 (μm)
Span : Off
Diameter on cumulative %
: 10.00(%) 8.9968 (μm)
: 50.00(%) 17.0694 (μm)
: 90.00(%) 161.0369 (μm)

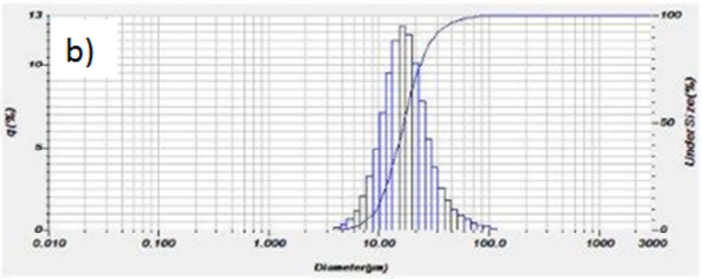

Median size : 16.8357 (μm)
Mean size : 19.6118 (μm)
Std. dev. : 11.7600 (μm)
Geo. mean size : 17.2085 (μm)
Geo. std. dev. : 1.6381 (μm)
Mode size : 16.2710 (μm)
Span : Off
Diameter on cumulative %
: 10.00(%) 9.4218 (μm)
: 50.00(%) 16.8357 (μm)
: 90.00(%) 31.9980 (μm)

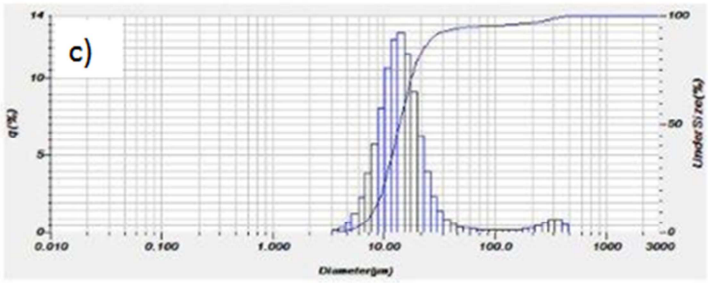

Median size : 13.9095 (μm)
Mean size : 27.4637 (μm)
Std. dev. : 59.6418 (μm)
Geo. mean size : 15.6955 (μm)
Geo. std. dev. : 2.1426 (μm)
Mode size : 14.1082 (μm)
Span : Off
Diameter on cumulative %
: 10.00(%) 7.9766 (μm)
: 50.00(%) 13.9095 (μm)
: 90.00(%) 27.5909 (μm)

Figure S5.6.2 Scanning electron micrographs of $CaCO_3$ crystals produced under and ultrasound irradiation at CO_2 flow-rates of d) 0.36 ℓ/min, e) 0.90 ℓ/min and f) 1.62 ℓ/min (Ca-rich solution containing 560 mmol/ℓ as Ca)